Cell Reports

Article

GSNOR deficiency promotes tumor growth via FAK1 S-nitrosylation

Graphical abstract

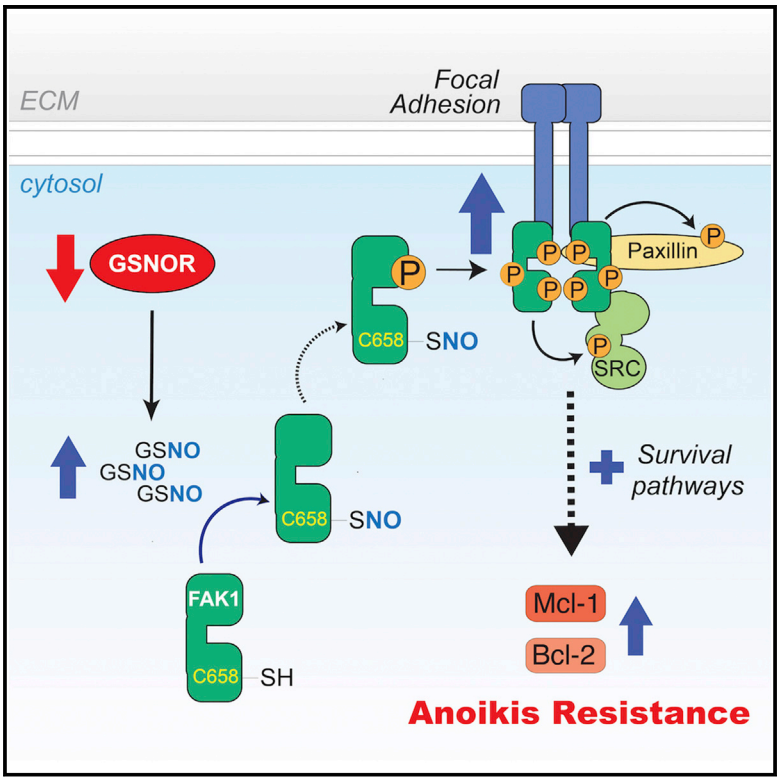

Highlights

- The denitrosylase GSNOR is hypo-expressed in several human cancers
- GSNOR decreases results in FAK1 S-nitrosylation on C459 and C658
- C658 S-nitrosylation stimulates FAK1 phosphorylation and confers anoikis resistance
- GSNOR deficiency sensitizes cells, organoids, and tumors to FAK1 inhibitors

Authors

Salvatore Rizza, Luca Di Leo, Chiara Pecorari, ..., Daniela De Zio, Blagoy Blagoev, Giuseppe Filomeni

Correspondence

rizza@cancer.dk (S.R.), giufil@cancer.dk (G.F.)

In brief

This study by Rizza et al. provides evidence of defects in the signaling of nitric oxide (NO) in several human cancers. This stimulates the activation of the oncogene FAK1, thus allowing cancer cells to elude cell death induced by detachment from extracellular matrix and give rise to bigger masses.

Rizza et al., 2023, Cell Reports *42*, 111997
January 31, 2023
https://doi.org/10.1016/j.celrep.2023.111997

CellPress

Cell Reports

CellPress
OPEN ACCESS

Article

GSNOR deficiency promotes tumor growth via FAK1 *S*-nitrosylation

Salvatore Rizza,[1,*] Luca Di Leo,[2] Chiara Pecorari,[1] Paola Giglio,[3] Fiorella Faienza,[3] Costanza Montagna,[3,4] Emiliano Maiani,[3,4] Michele Puglia,[5] Francesca M. Bosisio,[6] Trine Skov Petersen,[7] Lin Lin,[7,8] Vendela Rissler,[9,14] Juan Salamanca Viloria,[9] Yonglun Luo,[7,8,10] Elena Papaleo,[9,11] Daniela De Zio,[2,12] Blagoy Blagoev,[5] and Giuseppe Filomeni[1,3,13,15,*]

[1]Redox Biology, Danish Cancer Society Research Center, 2100 Copenhagen, Denmark
[2]Melanoma Research Team, Danish Cancer Society Research Center, 2100 Copenhagen, Denmark
[3]Department of Biology, University of Rome "Tor Vergata", 00133 Rome, Italy
[4]UniCamillus-Saint Camillus, University of Health Sciences, 00131 Rome, Italy
[5]Department of Biochemistry and Molecular Biology, University of Southern Denmark, 5230 Odense M, Denmark
[6]Lab of Translational Cell and Tissue Research, University of Leuven, 3000 Leuven, Belgium
[7]Department of Biomedicine, Aarhus University, 8000 Aarhus C, Denmark
[8]Steno Diabetes Center Aarhus, Aarhus University Hospital, 8200 Aarhus N, Denmark
[9]Cancer Structural Biology, Danish Cancer Society Research Center, 2100 Copenhagen, Denmark
[10]Lars Bolund Institute of Regenerative Medicine, Qingdao-Europe Advanced Institute for Life Sciences, BGI-Qingdao, BGI-Shenzhen, Shenzhen 518083, China
[11]Cancer Systems Biology, Section for Bioinformatics, Department of Health and Technology, Technical University of Denmark, 2800 Lyngby, Denmark
[12]Department of Drug Design and Pharmacology, Faculty of Health and Medical Sciences, Copenhagen University, 2100 Copenhagen, Denmark
[13]Center for Healthy Aging, Copenhagen University, 2200 Copenhagen, Denmark
[14]Present address: Division of Clinical Genetics, Department of Laboratory Medicine, Lund University, Lund 221 00, Sweden
[15]Lead contact
*Correspondence: rizza@cancer.dk (S.R.), giufil@cancer.dk (G.F.)
https://doi.org/10.1016/j.celrep.2023.111997

SUMMARY

Nitric oxide (NO) production in the tumor microenvironment is a common element in cancer. S-nitrosylation, the post-translational modification of cysteines by NO, is emerging as a key transduction mechanism sustaining tumorigenesis. However, most oncoproteins that are regulated by S-nitrosylation are still unknown. Here we show that S-nitrosoglutathione reductase (GSNOR), the enzyme that deactivates S-nitrosylation, is hypo-expressed in several human malignancies. Using multiple tumor models, we demonstrate that GSNOR deficiency induces S-nitrosylation of focal adhesion kinase 1 (FAK1) at C658. This event enhances FAK1 autophosphorylation and sustains tumorigenicity by providing cancer cells with the ability to survive in suspension (evade anoikis). In line with these results, GSNOR-deficient tumor models are highly susceptible to treatment with FAK1 inhibitors. Altogether, our findings advance our understanding of the oncogenic role of S-nitrosylation, define GSNOR as a tumor suppressor, and point to GSNOR hypo-expression as a therapeutically exploitable vulnerability in cancer.

INTRODUCTION

Cell adhesion to the extracellular matrix (ECM) is a physiological process mediated by integrins that maintains correct cytoskeleton assembly and generates signals that control cell migration, proliferation, and survival.[1,2] Malfunctioning cell-ECM interaction triggers *anoikis*, a form of apoptotic cell death that acts as a defense mechanism to limit misplaced re-adhesion of cells and their dysplastic growth.[3] Defective anoikis allows cells to survive in suspension and, in turn, concurs to the colonization of ectopic sites characterized by different ECM proteins, paving the way for cancer metastasis.[4] Anoikis resistance is indeed a distinctive signature of metastasizing cancer cells.

Several proteins implicated in cell adhesion to the ECM are directly involved in anoikis signaling. Among them, focal adhesion kinase-1 (FAK1) is commonly accepted as a central player. FAK1 is a non-receptor protein tyrosine kinase that acts as a hub, bridging integrins with a number of intracellular proteins, including paxillin and the oncoprotein tyrosine kinase Src (SRC) that together constitute the focal adhesion (FA) complex.[2,5] Upon interaction with the ECM, integrins clusterize and stimulate FAK1 to switch from a closed (inactive) to an open (active) state.[6] In the open state, FAK1 dimerizes and auto-phosphorylates at Y397. This event is preparatory for Src family members recruitment at the FA and the phosphorylation of FAK1 on three additional tyrosine residues, Y576, Y577, and Y925. Such

a multistep regulation of FAK1 by phosphorylation results in the enrollment of additional partners, which finally leads to the activation of pro-survival pathways.[7,8] Besides direct phosphorylation, FAK1's overall activity is also affected by post-translational modifications (PTMs) occurring on other FA components, such as phosphorylation,[9] lipidation,[10] and redox modifications.[11] Regarding this last class of PTMs, it has been reported that ECM/integrin interaction generates reactive oxygen species (ROS) at the FA.[4,12] ROS play an important role in cell adhesion by activating SRC[13] and the low-molecular weight protein tyrosine phosphatase (LMW-PTP), a small phosphatase that regulates SRC and FAK1 phosphorylation via dithiol-to-disulfide exchange of two vicinal cysteines.[14,15] A physiologically relevant function for redox-active cysteines in cell adhesion has also been proposed for other FA components occurring via the covalent binding to nitric oxide (NO), a reaction termed S-nitrosation or S-nitrosylation.[16] The crucial role of S-nitrosylation in cell adhesion is highlighted by the fact that integrins, via integrin-linked kinase (ILK) or FAK1, indirectly interact with NO synthases (NOSs), the enzymes that generate NO, suggesting that FA signaling is tightly associated with endogenous NO production.[17–19] This is especially important in the context of cancer biology, as abnormal NO signaling, by altering FA assembly and activity, contributes to tumor progression.[20,21] In support of this hypothesis, it has been shown that S-nitrosylation of SRC at cysteine 498 stimulates SRC kinase activity and, in turn, boosts cell invasion and anoikis resistance.[22,23] Aberrant NO signaling is often the result of NOS2 overexpression, which has been observed in many cancer types[24,25] and/or a reduced expression (and activity) of denitrosylases, the class of enzymes controlling/deactivating S-nitrosylation.[26] The hypo-expression of the denitrosylase GSNOR[27,28] is indeed associated with the onset and progression of hepatocellular carcinoma[29,30] and HER2$^+$ breast cancer.[31] We also revealed that GSNOR-deficient cells exhibit defective mitochondrial homeostasis,[32,33] a condition contributing to tumor metabolic rewiring that can be exploited for anticancer therapies.[34,35] Nevertheless, despite all these findings, a clear role for GSNOR and S-nitrosylation in tumor biology has not yet been established, and the effect of defective denitrosylation on FA signaling, in particular on FAK1 activity, has not been explored.

In this work, we investigate the molecular mechanisms through which S-nitrosylation, caused by GSNOR deficiency, regulates FAK1 activity and anoikis resistance, outlining a tumor suppressor role for GSNOR that can be exploited for personalized anticancer treatments.

RESULTS

GSNOR loss promotes tumor growth without affecting cell proliferation

GSNOR downregulation has been proposed to be associated with cancer onset and progression.[29–31] To extend the analysis of GSNOR expression in cancer, we analyzed the transcriptomic data deposited in The Cancer Genome Atlas (TCGA) and observed that GSNOR expression was significantly decreased in a wide variety of human cancers (Figure 1A). For a number of them, low GSNOR levels were associated with poor prognosis (Figures 1B and 1C), supporting the hypothesis that GSNOR hypo-expression typifies different molecular subtypes of cancer and might have a prognostic value. To explore the functional role of GSNOR in cancer, we generated GSNOR knockout (KO) HeLa and MCF7 cells by CRISPR-Cas9 technology, and GSNOR-deficient (knockdown [KD]) HepG2 by stable expression of short hairpin RNA (shRNA). Preliminary characterization of GSNOR-KO/KD cell lines showed that GSNOR loss did not significantly alter the expression of NOS2 and thioredoxin (TRX) (Figures S1A–S1C)—the only detectable NOS isoform and another abundant cellular denitrosylase, respectively—or the level of free NO (Figure S1D), which was kept sustained, and above the limit of detection, as usually reported in many cancer types. We next observed that GSNOR loss promoted HepG2 vertical growth; namely, it was associated with an increased size of overconfluent cell foci (see magnification of a focus in Figure 1D) and enhanced the colony-forming ability of HeLa cells (Figure 1E). These data suggested that GSNOR-deficient cells were not affected by contact inhibition and had acquired anchorage-independent growth ability. These phenotypes were associated with no changes in cell proliferation or viability (Figures S1E–S1G), and no alterations in the cell cycle (Figures S1H and S1I), except for a mild modulation of HepG2 cells in G1 and S phases, which was not correlated with an increase in nucleotide incorporation rate (Figure S1G). Coherently, tumor xenografts originating from GSNOR-KD HepG2 cells displayed faster growth kinetics and reached their maximum size earlier than parental controls (Figure 1F). Interestingly, they showed no modulation of Ki67 expression (Figure 1G), confirming that the tumorigenic potential of GSNOR-deficient cells was unrelated to cell proliferation.

GSNOR deficiency confers anoikis resistance

To understand the mechanisms linking GSNOR loss to increased tumorigenicity, we generated tumor organoids and analyzed the effects of GSNOR deficiency on their morphology and viability. Unexpectedly, microscopic examinations revealed that GSNOR-deficient cells gave rise to smaller spheroids (Figure 2A) with an almost perfectly rounded shape (Figure 2B). Intrigued by these results, we examined the viability of HeLa- and HepG2-derived spheroids using confocal fluorescence microscopy. GSNOR-KO/KD cells generated denser spheroids containing fewer dead cells, regardless of the number of cells seeded or spheroid size (Figures 2C and S2A). Three-dimensional (3D) reconstruction suggested that the apparent larger diameter of wild-type (WT) organoids was due to a collapse of the sphere into a flat cluster of dead cells, whereas GSNOR-deficient cells sustained the formation of solid and compact spheroids (Videos S1, S2, S3, and S4), which correlated with increased cell viability (Figure 2D). Similar results were also obtained by incubating HeLa cells with the reversible pharmacological inhibitor of GSNOR, N6022 (Figure S2B), and in other cancer cell lines that have the propensity to form tumor spheroids (renal carcinoma 769P and rhabdomyosarcoma RD cell lines) upon GSNOR silencing (Figure S2C). In MCF7 cells, which produce mammospheres when supplemented with a combination of hormones and growth factors, we found that GSNOR ablation stimulated the formation of viable mammospheres even in standard

CellPress
OPEN ACCESS

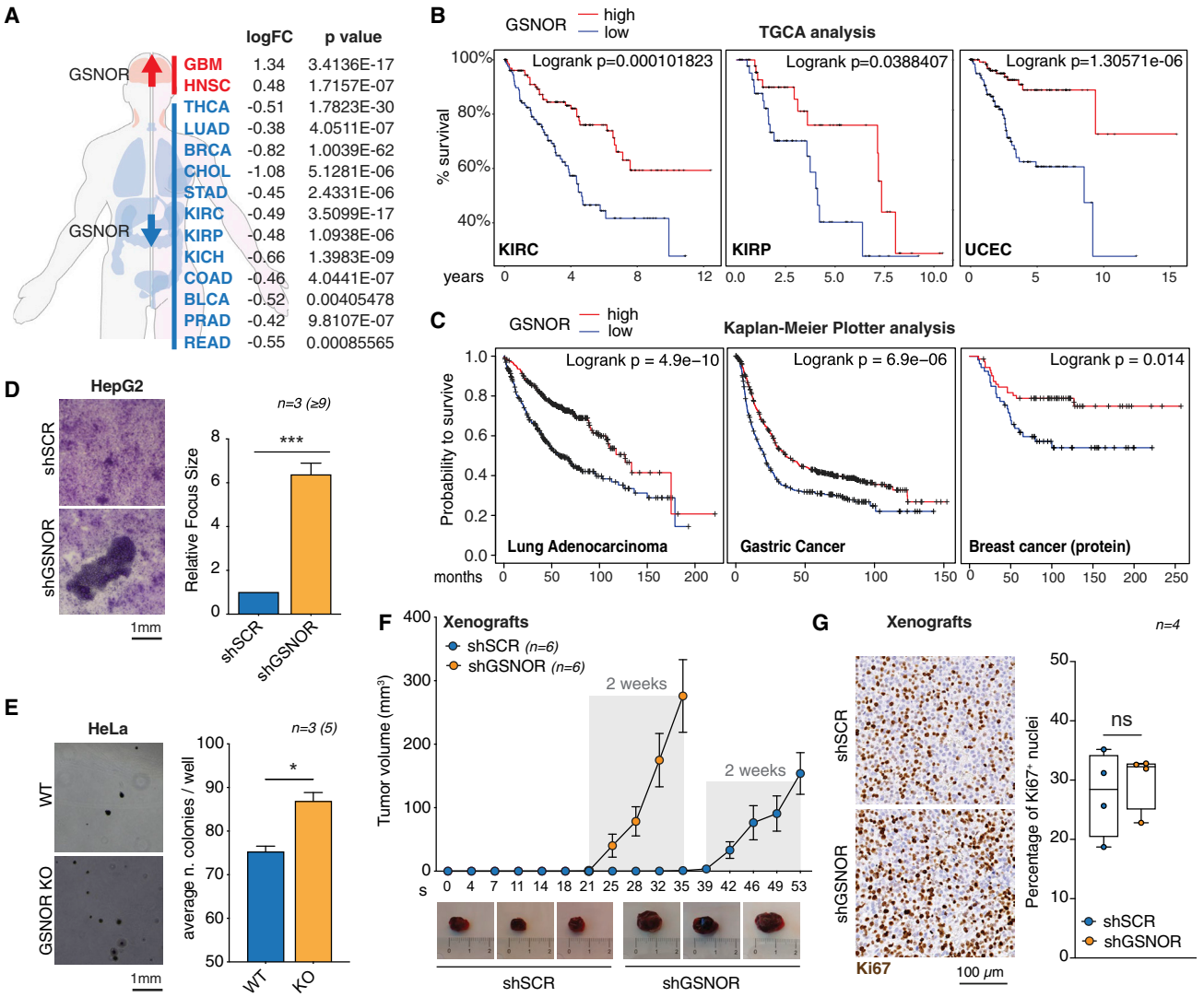

Figure 1. GSNOR loss promotes tumor growth without affecting cell proliferation

(A) Differential expression analysis of GSNOR in primary tumors versus paired normal tissue from TCGA database. Red, GSNOR-upregulating tumors; blue, GSNOR-downregulating tumors. Logarithmic fold change (logFC) of GSNOR expression and statistics significance (p value) are reported on the right.

(B and C) Kaplan-Meier survival analysis in GSNOR high-expressing (red line) or low-expressing (blue line) tumors calculated extracting clinical information from TCGA database (B) or the web-based analysis tool KMplot (C). Tumors were thresholded according to GSNOR mRNA or protein levels, as indicated. Survival is expressed as percentage (B) or as probability to survive (C).

(D) Representative images of overconfluent *GSNOR*-silenced (shGSNOR) and control (shSCR) HepG2 cells stained with Crystal violet (left). Histograms (right) shows the average relative size + SEM of cell foci.

(E) Representative images of colony-forming assay performed on *GSNOR*-null (GSNOR KO) and WT HeLa cells (left) and histograms (right) showing the average number of colonies/well + SEM (right).

(F) Volume assessment of shGSNOR and shSCR HepG2 xenografts (top). Highlighted in gray, the last 2 weeks of growth after tumors appearance. Representative images of 3 tumor masses for each genotype at the endpoint of the experiment (bottom).

(G) Ki67 immunostaining of HepG2 xenografts (left) and boxplots showing the percentage of Ki67$^+$ nuclei (right). n refers to biologically independent experiments or the number of animals per experimental group; numbers in parentheses represent technical replicates. In the boxplots, the center line shows the median, box limits are the 25th and 75th percentiles, and whiskers show minimum and maximum.

Data were analyzed using two-tailed unpaired (D and G) or paired (E) t test. ns, not significant. *p ≤ 0.05 and ***p ≤ 0.001. All raw data and statistics are reported in Table S1. See also Figure S1.

medium (Figures 2E–2G; Videos S5 and S6). Cell competency to form tumor spheroids strongly depends on the ability to escape anoikis and grow in an anchorage-independent manner.[3] Therefore, in light of our results, we investigated the effect of GSNOR loss on anoikis. Compared with their control counterparts, GSNOR-deficient cells (Figure 2H), or parental cells in the

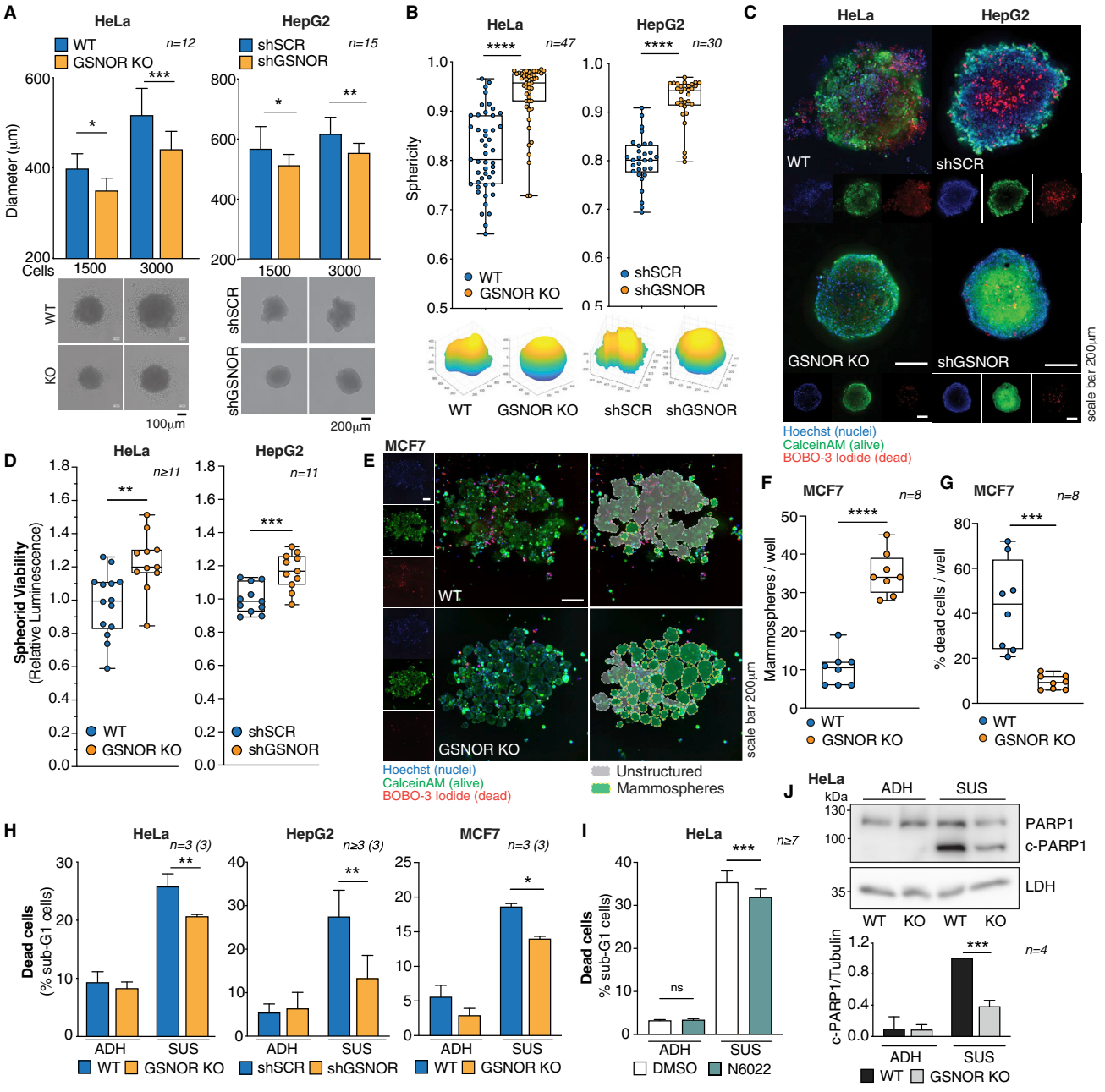

Figure 2. GSNOR deficiency confers anoikis resistance

(A) Diameter assessment (top) and representative bright-field images (bottom) of GSNOR-deficient versus WT spheroids generated by seeding 1,500 or 3,000 HeLa (left) or HepG2 cells (right).

(B) Sphericity index analysis of spheroids generated as in (A) (top). ReViSP[36] software was used to compute spheroids' 3D surface starting from bright-field images (bottom).

(C) Representative images (maximum projections of ≥10 z stacks of 10 µm) of GSNOR-deficient versus WT spheroids generated from HeLa (left) or HepG2 cells (right), acquired by confocal microscopy. Nuclei (blue) were stained with Hoechst 33342 and live (green) and dead (red) cells with CalceinAM and BOBO-3 iodide, respectively.

(D) Viability of GSNOR-deficient versus WT spheroids generated from HeLa (left) or HepG2 cells (right) was assessed using CellTiter 3D reagent and expressed as relative luminescence.

(E) Representative images of mammospheres generated from GSNOR-KO and WT MCF7 stained and acquired as in (C). On the right, mammospheres are highlighted in green circles whereas unstructured cell clumps are in gray.

(F and G) Boxplots showing the number of mammospheres per well (F) and the percentage of dead cells (G) calculated as ratio between dead (BOBO-3 iodide$^+$) and total cells (Hoechst$^+$) as in (E).

(legend continued on next page)

CellPress
OPEN ACCESS

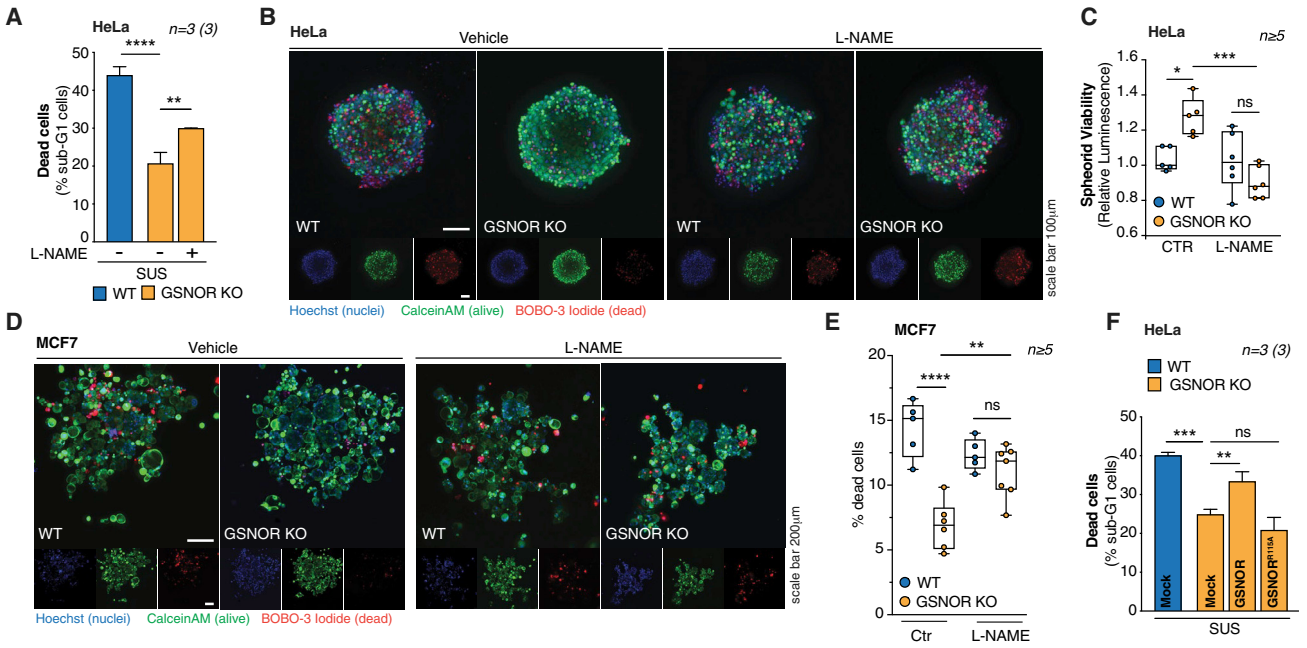

Figure 3. Anoikis resistance of GSNOR-deficient cells depends on S-nitrosylation

(A) Flow cytometry evaluation of dead cells of GSNOR-KO and WT HeLa cells grown in adherence (ADH) or in suspension (SUS) for 48 h with or without L-NAME 500 µM upon staining with propidium iodide.

(B and D) Representative confocal microscopy images of GSNOR-KO versus WT spheroids generated from HeLa (B) or MCF7 (D) with or without L-NAME 500 µM, acquired by confocal microscopy. Nuclei (blue) were stained with Hoechst 33342 and live (green) and dead (red) cells with CalceinAM and BOBO-3 iodide, respectively.

(C and E) Boxplot showing spheroid viability of HeLa-derived (C) and MCF7-derived (E) spheroids shown in (B) and (D), assessed using CellTiter 3D reagent, and expressed as relative luminescence.

(F) Flow cytometry evaluation of cell death after 48 h of forced suspension (SUS) in WT and GSNOR-KO HeLa cells upon reintroduction of fully functional (GSNOR) or the catalytically inactive mutant (GSNOR^{R115H}) of GSNOR. n refers to biologically independent experiments; numbers in parentheses represent technical replicates. In the boxplots, center line shows the median, box limits are the 25th and 75th percentiles, and whiskers show minimum and maximum.

Histograms represent mean ± SEM (A, F). Data were analyzed using one-way ANOVA followed by Sidak's multiple-comparisons test. ns, not significant. *p ≤ 0.05, **p ≤ 0.01, ***p ≤ 0.001, and ****p ≤ 0.0001. All raw data and statistics are reported in Table S1. See also Figure S3.

presence of GSNOR inhibitor (Figure 2I), were resistant to anoikis, showed reduced PARP1 cleavage (a marker of late apoptosis) (Figures 2J and S2D) and increased viability (Figure S2E) when grown in forced suspension. In agreement, the pan-caspase inhibitor ZVAD reduced apoptotic cells in both parental and GSNOR-KO cells forced to grow in suspension (Figure S2F). Interestingly, staurosporine (a canonical apoptotic stimulus) induced apoptosis to the same extent in both GSNOR-KO and parental control cells (Figures S2G and S2H), indicating that the apoptotic machinery was unaffected by GSNOR loss but differently responsive to anoikis stimuli.

S-nitrosylation is required for the anoikis resistance of GSNOR-deficient cells

GSNOR is a prototypical denitrosylase that regulates protein S-nitrosylation. To verify the role of S-nitrosylation in the anoikis resistance observed in GSNOR-deficient cells, we inhibited NO biosynthesis by treating the cells with sublethal concentrations of the pan-NOS inhibitor L-NAME (Figure S3A). Fluorometric and confocal microscopy analyses revealed that L-NAME rescued responsiveness to anoikis in GSNOR-deficient cells (Figures 3A and S3B) and organoids (Figures 3B–3E, S3C, and S3D). Analogously, reintroducing a fully functional (WT), but not

(H) Flow cytometry evaluation of sub-G1 (dead) cells upon staining with propidium iodide of GSNOR-deficient and WT HeLa (left), HepG2 (middle), and MCF7 cells (right) grown in adherence (ADH) or in suspension (SUS) for 48 h.

(I) Flow cytometry evaluation of sub-G1 (dead) cells upon staining with propidium iodide of HeLa cells grown in adherence (ADH) or in suspension (SUS) for 48 h in the presence of 5 µM N6022 or a vehicle solution (DMSO).

(J) Western blot of PARP1 and LDH (loading control) in GSNOR-KO and WT HeLa cells grown in adherence (ADH) or in suspension (SUS) for 48 h. Quantifications of western blots are shown at the bottom. n refers to biologically independent experiments; numbers in parentheses represent technical replicates. In the boxplots, center line shows the median, box limits are the 25th and 75th percentiles, and whiskers show minimum and maximum.

Histograms represent mean ± SEM (H) or mean ± SD (A and J). Data were analyzed using one-way ANOVA followed by Sidak's multiple-comparisons test (A, H, and I) and two-tailed unpaired (B and D) or paired (I) t test. ns, not significant. *p ≤ 0.05, **p ≤ 0.01, ***p ≤ 0.001, ****p ≤ 0.0001. All raw data and statistics are reported in Table S1. See also Figure S2.

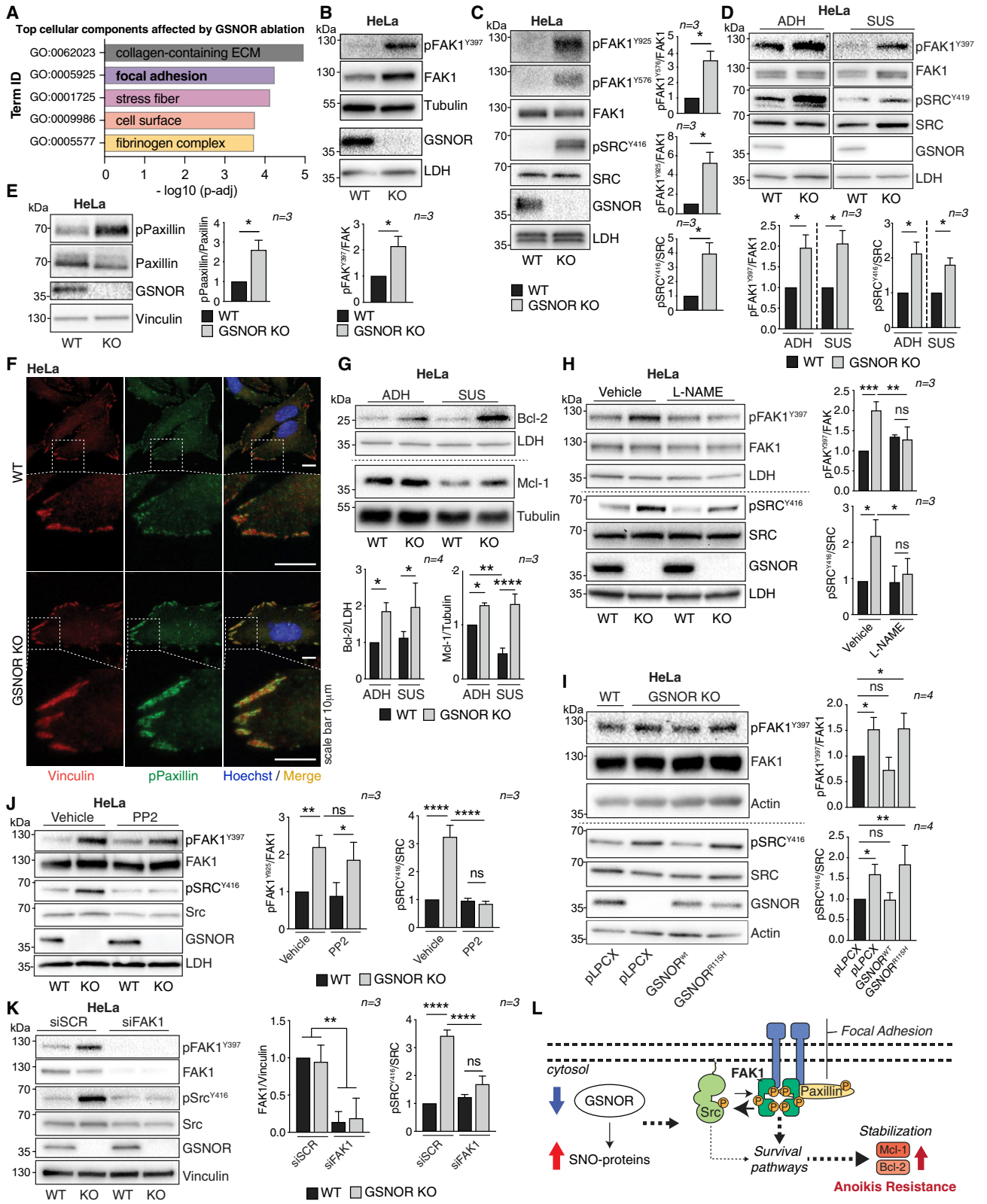

(legend on next page)

the catalytically inactive R115H mutant of GSNOR into GSNOR-KO cells restored anoikis sensitivity (Figure 3F). It is worth noting that the overexpression of GSNOR did not per se induce cell death in adherent cells or anoikis when they were forced to grow in suspension (Figure S3E). Together with the results previously obtained with the GSNOR inhibitor, these findings further indicate that GSNOR loss led to anoikis evasion via S-nitrosylation.

GSNOR downregulation alters focal adhesion signaling

Searching for the molecular event driving anoikis resistance, we performed RNA sequencing analyses of GSNOR-KO and WT HeLa cells. Results obtained showed that GSNOR loss was associated with changes in the expression of 286 genes (Figure S4A). Investigation of differentially expressed genes revealed that collagen-containing ECM and focal adhesion, which are the key regulators of anoikis, were the major cell components modulated upon GSNOR ablation (Figure 4A). On the basis of these results, we investigated the effects of GSNOR deficiency on FAK1 signaling. Western blot analyses of GSNOR-KO cells, or WT cells treated with the GSNOR inhibitor N6022, revealed a significant increase in the phosphorylation levels of FAK1 at Y397 and SRC, the principal functional interactor of FAK1 at the FA (Figures 4B, 4C, and S4B–S4E). In GSNOR-deficient HeLa and HepG2 cells, FAK1 was also phosphorylated at Y576, Y577, and Y925 (Figures 4C and S4B), two residues modified by SRC, and other Src kinase family members, upon interaction with phosphorylated Y397. Notably, FAK1 and SRC phosphorylation were maintained sustained in HeLa cells forced to grow in suspension (Figure 4D), a condition in which FAK1 signaling is normally inhibited. As an indication of FAK1 activation, we observed that paxillin, one well-known target of FAK1, was massively phosphorylated at the FA of GSNOR-KO cells (Figures 4E, 4F, and S4F). Moreover, the levels of the anti-apoptotic proteins Bcl2 and Mcl-1 were maintained even when cells were forced to suspension (Figure 4G), strengthening the idea that GSNOR deficiency hyperactivated FA signaling and stimulated pro-survival pathways.[37,38] FAK1 and SRC phosphorylation was prevented by L-NAME (Figure 4H) or by the re-introduction of GSNOR WT, but not by the R115H mutant (Figure 4I), indicating that S-nitrosylation is essential for FAK1-SRC complex activation.

FAK1 activation by autophosphorylation at Y397 takes place without the involvement of SRC (and any other member of the Src family), which, instead, is reported to phosphorylate FAK1 at Y576, mainly following autophosphorylation at Y397.[5] Even though we found both FAK1 and SRC phosphorylated in GSNOR-deficient cells, the pharmacological inhibition of SRC with three different Src family inhibitors (PP2, saracatinib, and dasatinib) had no effect on FAK1 autophosphorylation (Figures 4J, S4G, and S4H), whereas FAK1 silencing completely prevented SRC from getting phosphorylated (Figure 4K). Overall, these data support the idea that GSNOR loss results in FAK1 activation in a SRC-independent manner, and represents the main upstream event stimulating pro-survival pathways leading to anoikis resistance (see model in Figure 4L).

GSNOR deficiency promotes FAK1 *S*-nitrosylation

Data so far provided argued for FAK1 signaling activation being a common trait of GSNOR-deficient cells and suggested that S-nitrosylation represents the molecular mechanism underlying this phenomenon by directly targeting FAK1. To test this hypothesis, we chose GSNOR-KO HeLa cells as an elective model. Biotin switch assays revealed a significant increase in the S-nitrosylated (SNO) form of FAK1 (Figure 5A). By analyzing the FAK1 amino acid sequence using GPS-SNO software,[39] we predicted C459 and C658 as potential targets of S-nitrosylation (Figure 5B). Interestingly, C658 is conserved among the Src kinase family members and corresponds to C498 in SRC, the residue previously identified as an SNO target[22] (Figure S5A). We then sought to identify the SNO-cysteine(s) in FAK1 by stimulating SNO formation using the NO donor PAPA NONOate in batch (i.e., in lysates of HeLa cells overexpressing the WT form, as well as the single C459A and C658S or the double C458A-C658S mutants of FAK1). Biotin switch assays revealed that both C459 and C658 were targets of S-nitrosylation, with C658 accounting for the majority of the

Figure 4. GSNOR downregulation alters focal adhesions signaling

(A) Analysis of differentially expressed genes showing the major cell components modulated in GSNOR-KO versus WT cells, ranked from the top to the bottom according to statistical significance expressed as $-\log_{10}$(adjusted p value).

(B, C, and E) Western blots of the basal and phosphorylated forms of FAK1, SRC (B and C), paxillin (E), and GSNOR in extracts from GSNOR-KO and WT HeLa cells grown in adherence. Densitometry is shown at the bottom (B) or on the right (C and E).

(D) Western blots of GSNOR along with the basal and phosphorylated forms of FAK1 and SRC in GSNOR-KO and WT HeLa cells grown in adherence (ADH) or in suspension (SUS) for 48 h. Densitometry is shown at the bottom.

(F) Representative immunofluorescence images of GSNOR-KO and WT HeLa cells stained with Hoechst 33342 (nuclei, blue), an anti-vinculin (red), and an anti-phosphorylated paxillin antibody (green). Dotted squares highlight the areas of magnification (5×) on the bottom.

(G) Western blot of Bcl2 and Mcl-1 in GSNOR-KO and WT HeLa cells grown in adherence (ADH) or in suspension (SUS) for 48 h. Densitometry is shown on the bottom.

(H and I) Western blots of GSNOR along with the basal and phosphorylated forms of FAK1 and SRC in GSNOR-KO and WT HeLa cells treated or not with L-NAME 500 μM for 48 h (H) or transfected with a fully functional (WT) or the R115H mutant of GSNOR into GSNOR-KO cells (I). Densitometry is shown on the right.

(J and K) Western blot of GSNOR along with the basal and phosphorylated forms of FAK1 and SRC in GSNOR-KO and WT HeLa cells upon 4 h treatment with the SRC inhibitor PP2 10 μM (J) or after 48 h of transfection with siFAK1 or a non-target RNA interference (siSCR) (K). Densitometry is shown on the right. Tubulin, LDH, actin or vinculin were alternatively used as loading controls.

(L) Schematic representation of the effect of GSNOR depletion (blue arrow) on the levels of nitrosylated proteins (SNO-proteins, red arrow) and focal adhesion signaling. GSNOR decrease stimulates the phosphorylation (P) of FAK1, SRC, and paxillin and the stabilization of anti-apoptotic Mcl-1 and Bcl2 (red arrow), thus conferring anoikis resistance. n refers to biologically independent experiments.

Histograms represent mean ± SD. Data were analyzed using two-tailed paired t test (B–E) or one-way ANOVA followed by Sidak's multiple-comparisons test (H–K). ns, not significant. *$p \leq 0.05$, **$p \leq 0.01$, ***$p \leq 0.001$, ****$p \leq 0.0001$. All raw data and statistics are reported in Table S1. See also Figure S4.

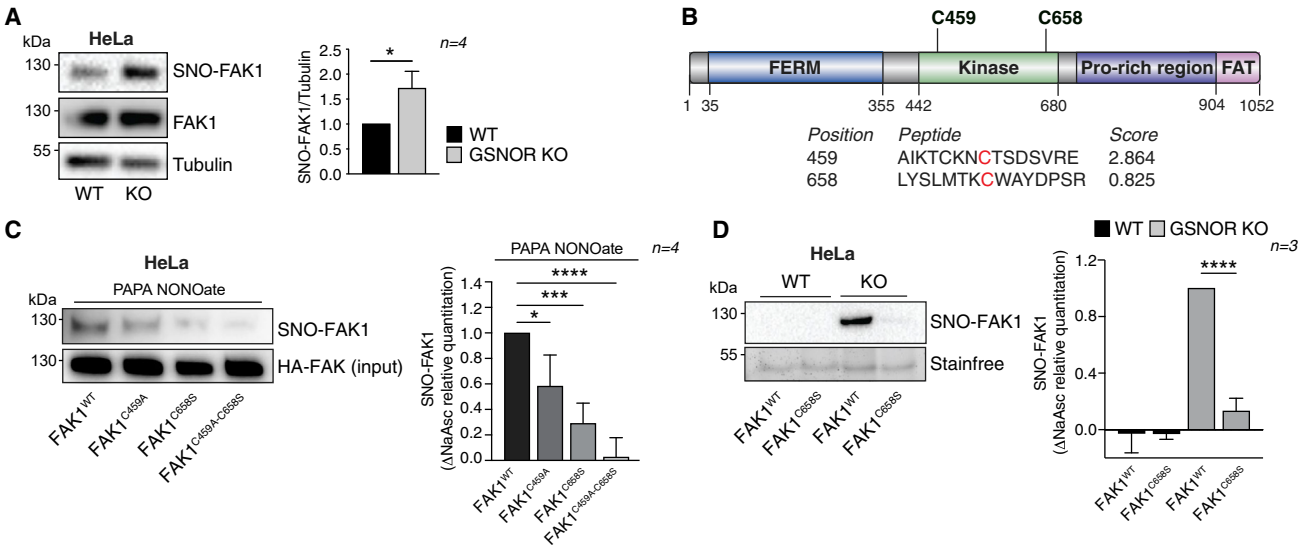

Figure 5. GSNOR deficiency promotes FAK1 S-nitrosylation

(A) Detection of S-nitrosylated FAK1 (SNO-FAK1) in protein extracts from GSNOR-KO and WT HeLa cells upon biotin switch assay, followed by FAK1 western blot. Tubulin was used as loading control. Densitometry is shown on the right.

(B) Top: schematic representation of FAK1 primary structure (top) showing the main protein domains (FERM, kinase, proline-rich region and FAT) and residues C459 and C658. Bottom: the sequences containing the two cysteines and the S-nitrosylation-propensity score (score) calculated by GPS-SNO software.

(C) SNO-FAK1 detected in cell extracts treated with PAPA NONOate 400 μM (30') obtained from HeLa cells overexpressing the HA-tagged wild-type (WT) FAK1 or the mutants C459A, C658S, or C459A-C658S. Samples were subjected to biotin switch assay, enriched in FAK1 by pull-down using streptavidin magnetic beads and revealed by an anti-HA antibody. Densitometry is shown on the bottom and represents the relative levels of SNO-FAK1 obtained in the presence of ascorbate (NaAsc) after subtracting the non-specific signal revealed in absence of ascorbate (ΔNaAsc).

(D) SNO-FAK1 detected in GSNOR-KO and WT HeLa cells overexpressing the HA-tagged wild-type (WT) FAK1 or the mutant C658S analyzed as in (C) (see densitometry on the bottom). n refers to biologically independent experiments.

Histograms represent mean ± SD. Data were analyzed using two-tailed paired t test (A) or one-way ANOVA followed by Sidak's multiple-comparisons test (C and D). ns, not significant. *p ≤ 0.05, **p ≤ 0.01, ***p ≤ 0.001, ****p ≤ 0.0001. All raw data and statistics are reported in Table S1. See also Figure S5.

detected signal (Figure 5C). In agreement, the levels of SNO-FAK1 were almost completely abolished in GSNOR-KO cells expressing the FAK1 C658S mutant (Figure 5D). It is worth noting that folding free energy calculations predicted that neither FAK1 C458A nor C658S substitutions altered the structural stability of the protein. (Figure S5B). Consistently, overexpression of HA-tagged FAK1 C458A and C658S mutants did not result in protein aggregates formations or affect subcellular localization, which indeed was distinctively kept at the focal adhesions (Figure S5C). Mass spectrometry (MS) analyses, carried out on immunoprecipitated FAK1 after in batch exposure to PAPA NONOate and subsequent biotinylation (Figure S5D), demonstrated unequivocally the presence of a biotinylation site at C458, but not at C658 (Figure S5E). Notably, C658 lies in close proximity to a trypsin cutting site. Therefore, the presence of a biotin group on C658 may prevent trypsin from recognizing and cleaving the sequence. As a result, the peptide bearing this modification is not produced and we could not detect it by MS. Both C459 and C658 lie in regions distant from most of the residues involved in the conformational changes associated with FAK1 activation. Consequently, any effect of S-nitrosylation on FAK1 phosphorylation should occur via long-range conformational changes. This hypothesis is supported by computational analyses based on Protein Structure Networks (PSN)[40] that show long-range structural changes propagating from C658, and not from C459, through the interface between the catalytic domain and the lobe F2 to other distal regions of the catalytic domain (Figure S5F).

FAK1 S-nitrosylation on C658 confers anoikis resistance

In agreement with the well-established oncogenic role of FAK1, we found that FAK1 silencing was extremely detrimental to our cell models, as it abolished the differences between WT and GSNOR-KO/KD cells growing in forced suspension. Cell viability was indeed equally affected (Figure 6A), and apoptotic markers were similarly activated (Figure S6A). By contrast, SRC inhibition had no effect (Figures S6B and S6C), confirming that FAK1 plays a primary role, whereas SCR only an auxiliary role, in the anoikis resistance observed in GSNOR-deficient cells. In line with these results, FAK1 knockout (FAK1-KO) in both WT and GSNOR-KO backgrounds (Figure S6D) showed that FAK1 was essential for the formation of well-defined (Figure 6B) and viable (Figure 6C) spheroids. On the contrary, dasatinib- and saracatinib-mediated SRC inhibition had no (or only minor) effects on spheroid viability (Figures S6E and S6F) and did not abolish differences between GSNOR-KO and WT cells. In the same settings, PP2 was per se too toxic and completely impaired spheroid formation (Figures S6G and S6H).

Finally, to determine the effects of S-nitrosylation on FAK1-mediated anoikis resistance, we introduced C459A or C658S

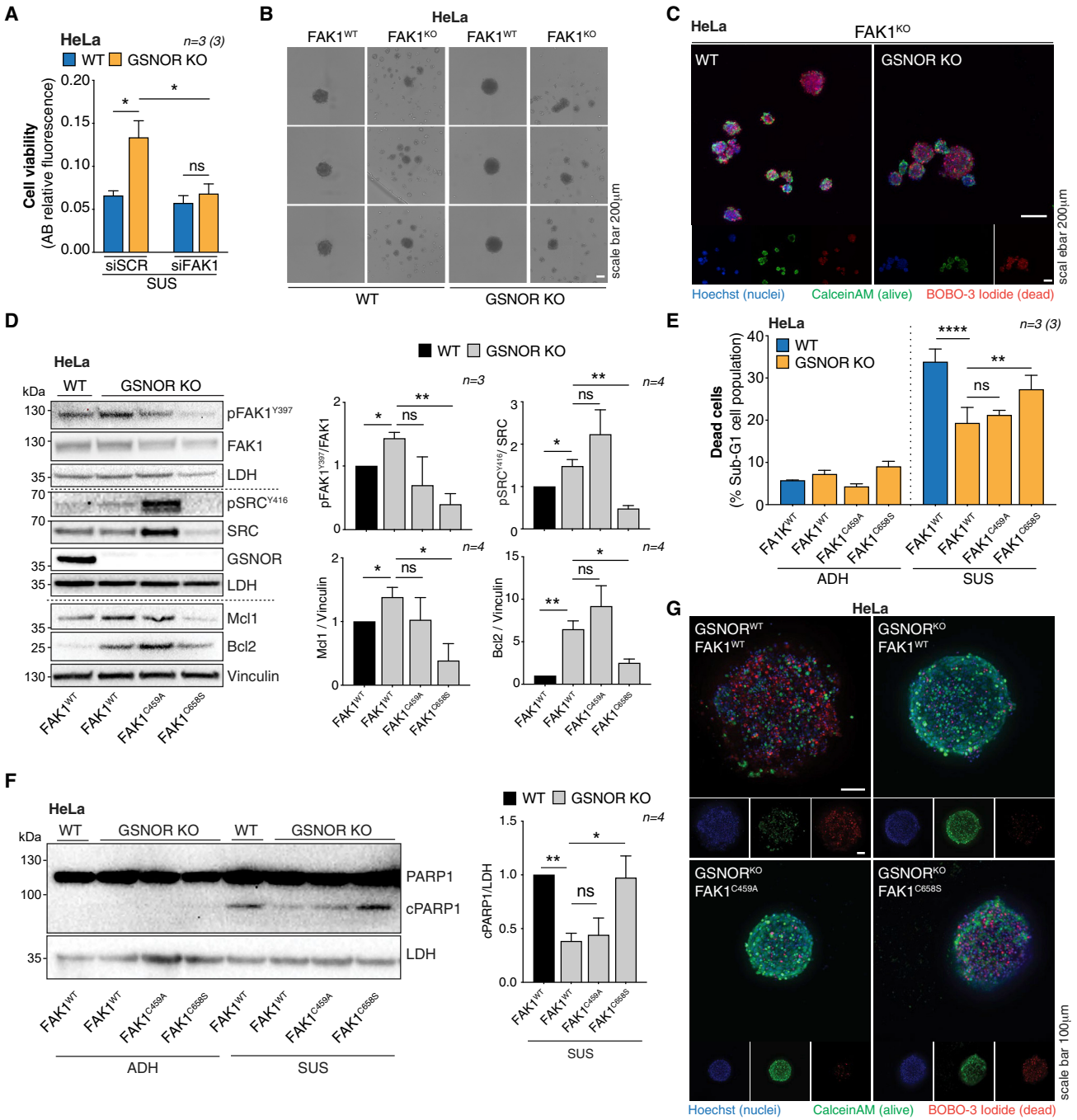

Figure 6. FAK1 S-nitrosylation on C658 confers anoikis resistance

(A) Cell viability, expressed as Alamar Blue (AB) relative fluorescence, of GSNOR-KO and WT HeLa cells transfected with siFAK1 or a non-target RNA interference (siSCR) and grown for 48 h in suspension (SUS).

(B and C) Representative bright-field (B) and fluorescence microscopy images (C) of GSNOR-KO and WT spheroids generated from HeLa cells expressing ($FAK1^{WT}$) or knocked out for FAK1 ($FAK1^{KO}$). In (C), images represent maximum projections of ≥10 z stacks of 10 µm. Nuclei were stained with Hoechst 33342 (blue) and live (green) and dead cells (red) with CalceinAM and BOBO-3 iodide, respectively.

(D) Western blots of GSNOR along with the basal and phosphorylated forms of FAK1 and SRC, Mcl-1, and Bcl2 in extracts from WT, GSNOR-KO, and GSNOR-KO HeLa cells endogenously expressing FAK1 C459A or FAK1 C658S. LDH and vinculin were used as loading controls. Densitometry is shown on the right.

(E and F) Flow cytometry evaluation of sub-G1 (dead) upon staining with propidium iodide (E) and western blot of PARP1 and LDH (F) from WT, GSNOR-KO, and GSNOR-KO cells endogenously expressing FAK1 C459A or FAK1 C658S and grown in adherence (ADH) or in suspension (SUS) for 48 h. Densitometry of (F) is shown on the right.

(legend continued on next page)

mutations on endogenous FAK1 by CRISPR-Cas9 technology (Figure S6I). This strategy allowed us to prevent C459 or C658 from undergoing S-nitrosylation and explore which of the two residues mainly affected FAK1 autophosphorylation in GSNOR-deficient conditions. In line with biotin switch assays, western blot analysis revealed that only the C658S substitution reduced FAK1 and SRC phosphorylation as well as the levels of Bcl2 and Mcl-1 proteins in GSNOR-KO cells (Figure 6D). C459A expression did not alter FAK1 autophosphorylation or FAK1 downstream signaling, as confirmed by Bcl2 and Mcl-1 levels (Figure 6D). However, for still unknown reasons, we observed an increase in the levels and phosphorylation of SRC. Consistently, cell death and PARP1 cleavage were restored (Figures 6E and 6F) and the viability of tumor organoids was reduced only in GSNOR-KO cells expressing the FAK1 C658S mutant (Figure 6G). By contrast, we observed that GSNOR-KO spheroids expressing the FAK1 C459A mutant, although smaller than those expressing the wild-type FAK1, did not die (Figure 6G). However, this phenomenon affected the absolute number of viable cells, resulting in an apparent reduction of cell viability (Figure S6J). Altogether, these data pointed to C658 as the effective S-nitrosylation target of FAK1, which is responsible for the anoikis evasion of GSNOR-deficient tumors.

GSNOR-deficient organoids and tumors are highly sensitive to FAK1 inhibition

With the aim of providing a clinical perspective to our findings, we examined the efficacy of two selective inhibitors of FAK1 (Y15 and defactinib) in reducing GSNOR-deficient tumor growth. Both molecules were effective in inhibiting FAK1 phosphorylation (Figures S7A and S7B), and GSNOR expression had little effect on the toxicity that they exhibited toward tumor cell lines grown in adhesion (Figures S7C–S7E). However, they significantly decreased tumor organoid viability, with the reduction being more pronounced in GSNOR-deficient backgrounds (Figures 7A, 7B, and S7F–S7H), mostly for Y15, which was therefore selected for next *in vivo* experiments. In particular, we monitored the growth of control (shSCR) and GSNOR-KD (shGSNOR) HepG2 tumor xenografts in NOG mice upon 14 days of treatment with Y15 (Figure 7C). Immunohistochemistry analyses confirmed Y15's ability to inhibit FAK1 phosphorylation at Y397 and Y567, with this effect being most pronounced in shGSNOR tumor xenografts (Figures S7I and S7J). In agreement, Y15 significantly decreased the weight and size of tumor xenografts compared with their shSCR control counterparts (Figures 7D and 7E). Microscopy analyses revealed that Y15 stimulated the formation of extensive TUNEL-positive regions in shGSNOR tumors, which were indicative of areas characterized by massive cell death (Figures 7F and 7G). This result was further confirmed by histopathological evaluations showing the formation of extensive necrotic and soft hemorrhagic stromal regions in shGSNOR tumor xenografts, which likely represented late-stage necrotic areas (Figures 7H and 7I). Overall, these results indicated that FAK1 inhibition may be a promising therapeutic strategy for selectively reducing the growth of GSNOR-deficient tumors.

DISCUSSION

FAK1 hyperactivation plays a crucial role in cancer biology, mainly in the tumor progression phase,[41] providing resistance to anoikis and boosting the ability of cancer cells to migrate and invade.[42] In this study, we provide the evidence for S-nitrosylation as post-translational modification that enhances FAK1 phospho-activation.

This result provides the molecular basis to decipher previous observations showing that triple Src, Lyn and Fyn KO (SYF) cells still showed FAK1 phosphorylation upon exposure to exogenous NO fluxes.[22] In particular, we propose that NO, via S-nitrosylation, can directly stimulate FAK1 autophosphorylation and drive anoikis resistance. Our findings point at C658 of FAK1 as a conserved site of S-nitrosylation (at position 498 in SRC) that potentiates FAK1 activity. Such consideration is of greater relevance in the context of cancer. Indeed, NO production and S-nitrosylation, are emerging as common elements in multiple models of tumor in which NOS is overexpressed[24,25] and GSNOR, as also confirmed in this work, downregulated.[29–31] However, targets remain poorly characterized. Unbiased proteomic screens have identified more than 20,000 S-nitrosylation sites in about 10,000 proteins, suggesting that more than 70% of the proteome may undergo S-nitrosylation. However, there is still no characterization or indication of how S-nitrosylation regulates the biological functions of most of these proteins. Herein, we have demonstrated that FAK1 undergoes S-nitrosylation at C658 (and to a much lesser extent at C459) in multiple GSNOR-deficient cancer models. Our data suggest that S-nitrosylation may act as a preparatory modification for phosphorylation, an interplay that amplifies the complexity of cell signaling and multi-level regulation of protein activities. This hypothesis finds support in a recent study showing that S-nitrosylation at C644 of DRP1, a small GTPase that mediates mitochondrial fragmentation, facilitates its phosphorylation at S616 in neurons,[43] thus extending the biological relevance of S-nitrosylation/phosphorylation crosstalk beyond cancer pathophysiology.

The precise mechanism by which C658 nitrosylation changes FAK1 structure and contributes to FAK1 phosphorylation remains unknown. Our initial computational analyses might suggest that it occurs through long-range conformational changes affecting the structure of FAK1 in regions far from this residue. For now, we can just speculate that S-nitrosylation interferes with the auto-inhibitory state of the protein (i.e., by weakening the interaction between the *FERM* and the kinase domains) or positively affect its binding with SRC. Results obtained upon treatment with Src family inhibitors lead us to rule out the latter

(G) Representative fluorescence microscopy images of spheroids derived from WT, GSNOR-KO, and GSNOR-KO endogenously expressing FAK1 C459A or FAK1 C658S HeLa cells. Images represent maximum projections of $\geq$10 z stacks of 10 μm, and cells were stained as in (B). n refers to biologically independent experiments, while numbers in parentheses represent technical replicates.

Histograms represent mean ± SEM (A and E) or mean ± SD (D and F). Data were analyzed using two-way ANOVA followed by Sidak's multiple-comparisons test. ns, not significant. *p $\leq$ 0.05, **p $\leq$ 0.01, ***p $\leq$ 0.001, ****p $\leq$ 0.0001. All raw data and statistics are reported in Table S1. See also Figure S6.

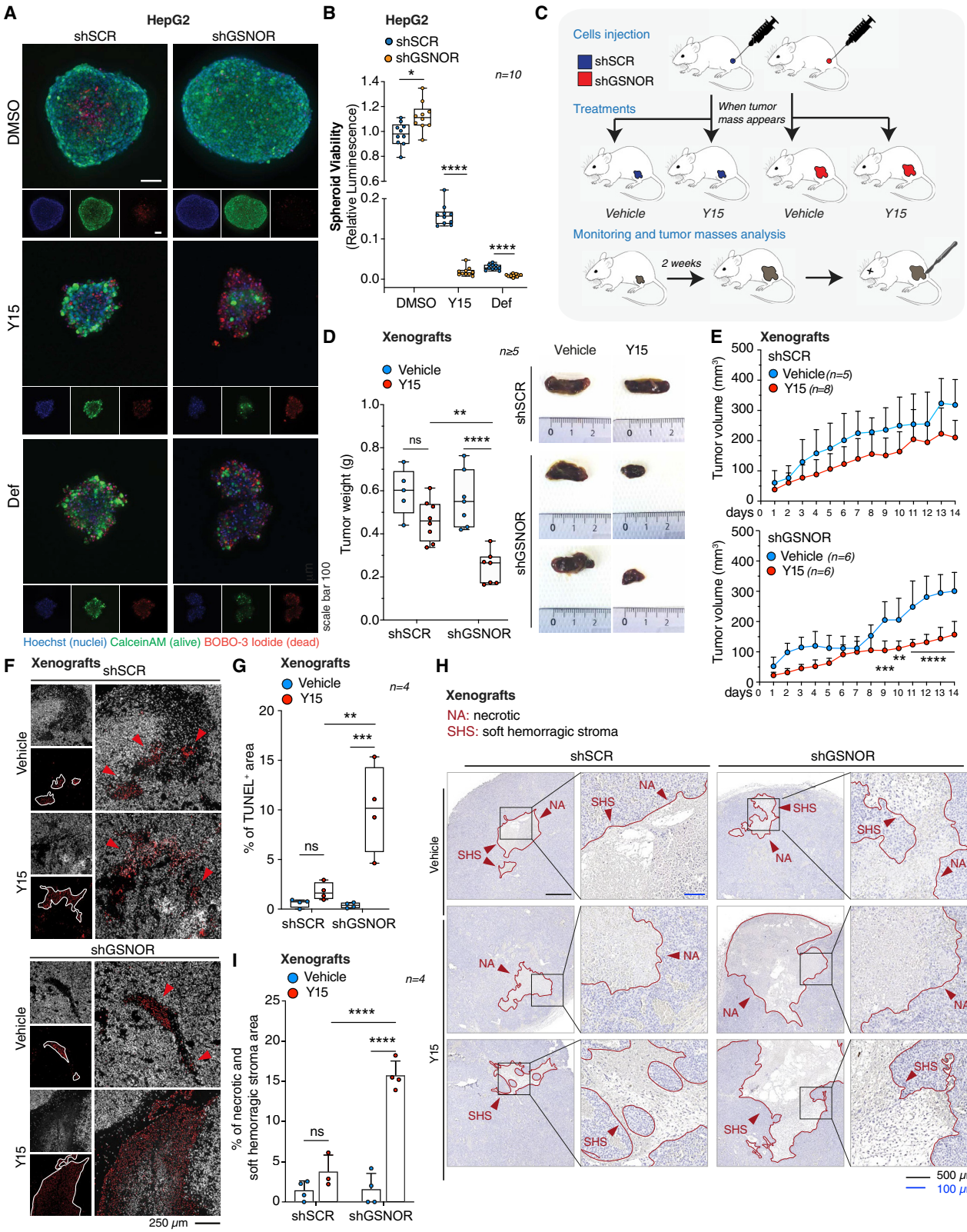

(legend on next page)

hypothesis as, in GSNOR-deficient cells, FAK1 phosphorylation seems to be mostly SRC independent. Alternatively, C658 nitrosylation could keep FAK1 in a phosphorylated and active state, preserving it from dephosphorylation (i.e., by affecting FAK1 recognition by LMW-PTP). Whatever the mechanism, it exclusively involves C658, as C459 nitrosylation does not seem to play any role in anoikis resistance. However, C459A mutants generate smaller organoids, suggesting that S-nitrosylation may affect other kinase-independent roles of FAK1 (i.e., the regulation of FA assembly and turnover, and the interaction with the cytoskeleton), which are all properties deregulated in cell migration and epithelial-to-mesenchymal transition.[41,44] We believe that an investigation of the role of FAK1 S-nitrosylation (and specifically at C459) in these processes needs extensive and dedicated work. Nonetheless, the findings here reported point to FAK1 as an elective target for the treatment of malignancies characterized by GSNOR loss, which we identified in this study as a feature of several cancers characterized by poor prognosis.

Several FAK1 inhibitors are currently in preclinical and clinical trials, either alone or in combination with SRC inhibitors, cytotoxic drugs, and anti-angiogenic agents.[45–47] However, their limited selectivity due to the residual effect that they still have on other Scr kinase family members and the non-receptor tyrosine kinase PYK2 (also known as FAK2),[45,48,49] makes this therapeutic strategy challenging. Furthermore, the inhibition of FAK1 kinase activity does not affect the aforementioned kinase-independent functions of FAK1.[44] Therefore, a thorough understanding of FAK1 regulation and cellular signaling circuits in different cancer types is essential to designing successful therapies. Within this framework, GSNOR expression may be used to stratify cancer patients for treatment with FAK1 inhibitors. Indeed, we show that mouse xenografts and organoids derived from GSNOR-deficient cells are particularly vulnerable to competitive (defactinib) and non-competitive (Y15) FAK1 inhibitors. The same may apply to other, much better characterized cancer types in which S-nitrosylation is deregulated because of NOS2 overexpression, a condition that typifies, among others, breast, ovarian, and liver cancers.[24,50,51]

Limitations of the study

The biotin switch assay (i.e., the substitution of an NO moiety with a biotin group on an S-nitrosylated cysteine) is, nowadays, one of the few indirect (and not very efficient) techniques used to analyze protein S-nitrosylation, as SNO adducts are particularly unstable throughout the sample processing period. The use of this method to measure FAK1 S-nitrosylation is therefore a point of concern in this study. A comprehensive analysis of the molecular dynamics of FAK1 intra-domain conformation upon S-nitrosylation is also missing. Because of the complexity of the protein architecture, a completely separate study is required to simulate the relevant conformational changes that are induced by S-nitrosylation on long timescales.

STAR★METHODS

Detailed methods are provided in the online version of this paper and include the following:

- KEY RESOURCES TABLE
- RESOURCE AVAILABILITY
  - Lead contact
  - Materials availability
  - Data and code availability
- EXPERIMENTAL MODEL AND SUBJECT DETAILS
  - Cell lines and spheroids
  - Animal model
- METHOD DETAILS
  - Reagents and treatments
  - Transient transfections and plasmids
  - Generation of FAK1 point mutations in cells
  - Analysis of cell death, viability, and proliferation
  - Tumorigenesis assays
  - Western blot analyses
  - Detection of S-nitrosylated proteins (biotin-switch assay)
  - FAK1 immunoprecipitation and mass spectrometry
  - Nitric oxide detection
  - Xenograft model and treatments

Figure 7. GSNOR-deficient organoids and tumors are highly sensitive to FAK1 inhibition

(A and B) Representative fluorescence microscopy images (A) and viability assay (B) of spheroids derived from GSNOR-deficient (shGSNOR) and control (shSCR) HepG2 cells upon treatment with Y15 2.5 μM, defactinib (DEF) 10 μM or vehicle (DMSO) every 48 h for 1 week. Images in (A) represent maximum projections of ≥10 z stacks of 10 μm. Nuclei were stained with Hoechst 33342 (blue) and live (green) and dead (red) cells with CalceinAM and BOBO-3 iodide, respectively.

(C) Schematic representation of the *in vivo* experiment aimed at testing the effects of Y15 treatment on the growth of GSNOR-deficient (shGSNOR) and control (shSCR) HepG2-derived xenografts. Xenografts were produced by injecting 5×10^6 cells on the right flank of each mouse. When tumor masses appeared, mice were separated in two groups: vehicle- and Y15-treated mice. Tumor volume was measured daily and after 2 weeks of treatment, mice were sacrificed, and xenografts surgically resected for further analysis.

(D) Tumor mass weight (left) and representative images (right) of shGSNOR and shSCR HepG2 mouse xenografts at the endpoint of treatment with 15 mg/kg Y15 or vehicle (saline solution) administered daily for 14 days after tumor mass appearance.

(E) Daily assessment of the volume of shGSNOR and shSCR HepG2 xenografts over treatment as in (C).

(F and G) Fluorescence microscopy images (F) of tumor sections from (C) stained with Hoechst 33342 (white) and TUNEL Assay Kit-BrdU (red). $TUNEL^+$ areas are highlighted by a white line in the red channel and indicated by red arrows in the merged image. The percentage of $TUNEL^+$ area/section is reported in (G).

(H and I) Hematoxylin and eosin (H&E)-stained sections (H) of the tumor masses described in (D). Necrotic (NA) and soft hemorrhagic stroma (SHS) areas are encircled by a red line and indicated by red arrows. Squares show the regions magnified (5×) on the right. The percentage of NA and SHS area/section is reported in (I). n refers to biologically independent experiments or the number of animals per experimental group. In the boxplots, center line shows the median, box limits are the 25th and 75th percentiles, and whiskers show minimum and maximum.

Data were analyzed using two-way ANOVA followed by Sidak's multiple-comparisons test. ns, not significant. *$p \leq 0.05$, **$p \leq 0.01$, ***$p \leq 0.001$, and ****$p \leq 0.0001$. All raw data and statistics are reported in Table S1. See also Figure S7.

- Immunohistochemistry (IHC)
- TUNEL assay
- Confocal fluorescence microscopy
- Analysis from The Cancer Genome Atlas
- Molecular modeling of FAK1 full-length
- RNA sequencing analysis

- QUANTIFICATION AND STATISTICAL ANALYSIS

SUPPLEMENTAL INFORMATION

Supplemental information can be found online at https://doi.org/10.1016/j.celrep.2023.111997.

ACKNOWLEDGMENTS

We are grateful to Laila Fisher for her secretarial work. We would like to acknowledge Matteo Lambrughi, Maria Francesca Allega, and Emmanuelle Bignon for discussion and involvement in the early stages of FAK1 molecular modeling; Søs Grønbæk Holdgaard, Mette Vixø Vistesen, and Chloé Duculty for experimental support; and Vanda Turcanova for lab assistance. This work was supported by grants from the Danish Cancer Society (KBVU R146-A9414 and R231-A13855 to G.F., R204-A12424 to D.D.Z.), the Italian Association for Cancer Research (IG2017-20719 to G.F.), the LEO Foundation (LF-OC-19-000004 to D.D.Z.), and the Novo Nordisk Foundation (NNF18OC0052550 to G.F., NNF18OC0052768 to B.B.). The work was also supported in part by the Danish National Research Foundation (DNRF; grant 141 to ATLAS) and the INTEGRa research infrastructure funded by NNF. D.D.Z. is supported by the Melanoma Research Alliance young investigator grant (MRA 620385), C.P. is a recipient of a PhD fellowship from the Danish Cancer Research Foundation (Dansk Kraeft-forskningsfond, DKF-0-0-532), F.F. is supported by an AIRC Fellowship for Italy, and E.M. and C.M. are supported by Fondazione Umberto Veronesi. L.L. is supported by Independent Research Fund Denmark – Sapere Aude Starting Grant (8048-00072A) and the Novo Nordisk Foundation (NNF21OC0071718). CRISPR gene editing in the laboratory of Y.L. is partially supported by the European Union's Horizon 2020 research and innovation program under grant agreement 899417. Cancer Structural Biology, Redox Biology, and Melanoma Research Team labs are part of the Center of Excellence for Autophagy, Recycling and Disease (CARD), funded by Danmarks Grundforskningsfond (DNRF125).

AUTHOR CONTRIBUTIONS

S.R. and G.F. conceived the study and designed experiments. S.R., C.P., P.G., and E.M. carried out the biochemical and microscopy experiments. S.R. and C.P. prepared samples for RNA sequencing (RNA-seq) and analyzed the data. P.G., F.F., and C.M. performed biotin switch assays. M.P. and B.B. designed and performed mass spectrometry analysis. S.R., L.D.L., and D.D.Z. designed and carried out xenograft experiments. L.D.L. performed immunohistochemistry analysis on tumor sections. F.M.B. performed the histopathological evaluation of tumor xenografts. T.S.P., L.L., and Y.L. designed and established FAK1 knockout and mutant-FAK1 cell lines by CRISPR-Cas9. E.P. and V.R. investigated GSNOR expression on TGCA database. E.P. and J.S.V. worked on FAK1 3D structure and meta-paths analysis. L.D.L. and E.M. provided critical support, key data analyses, and conceptual advice. S.R. and G.F. wrote the original draft. S.R. organized and archived unprocessed data and figures. All authors took part in reviewing and editing the final manuscript. All authors read and accepted the manuscript.

DECLARATION OF INTERESTS

The authors declare no competing interests.

INCLUSION AND DIVERSITY

We support inclusive, diverse, and equitable conduct of research.

Received: August 8, 2022
Revised: November 15, 2022
Accepted: January 4, 2023

REFERENCES

1. Zhou, D.W., Fernández-Yagüe, M.A., Holland, E.N., García, A.F., Castro, N.S., O'Neill, E.B., Eyckmans, J., Chen, C.S., Fu, J., Schlaepfer, D.D., and García, A.J. (2021). Force-FAK signaling coupling at individual focal adhesions coordinates mechanosensing and microtissue repair. Nat. Commun. *12*, 2359. https://doi.org/10.1038/s41467-021-22602-5.
2. Michael, K.E., Dumbauld, D.W., Burns, K.L., Hanks, S.K., and García, A.J. (2009). Focal adhesion kinase modulates cell adhesion strengthening via integrin activation. Mol. Biol. Cell *20*, 2508–2519. https://doi.org/10.1091/mbc.E08-01-0076.
3. Chiarugi, P., and Giannoni, E. (2008). Anoikis: a necessary death program for anchorage-dependent cells. Biochem. Pharmacol. *76*, 1352–1364. https://doi.org/10.1016/j.bcp.2008.07.023.
4. Paoli, P., Giannoni, E., and Chiarugi, P. (2013). Anoikis molecular pathways and its role in cancer progression. Biochim. Biophys. Acta *1833*, 3481–3498. https://doi.org/10.1016/j.bbamcr.2013.06.026.
5. Mitra, S.K., Hanson, D.A., and Schlaepfer, D.D. (2005). Focal adhesion kinase: in command and control of cell motility. Nat. Rev. Mol. Cell Biol. *6*, 56–68. https://doi.org/10.1038/nrm1549.
6. Lietha, D., Cai, X., Ceccarelli, D.F.J., Li, Y., Schaller, M.D., and Eck, M.J. (2007). Structural basis for the autoinhibition of focal adhesion kinase. Cell *129*, 1177–1187. https://doi.org/10.1016/j.cell.2007.05.041.
7. Brami-Cherrier, K., Gervasi, N., Arsenieva, D., Walkiewicz, K., Boutterin, M.C., Ortega, A., Leonard, P.G., Seantier, B., Gasmi, L., Bouceba, T., et al. (2014). FAK dimerization controls its kinase-dependent functions at focal adhesions. EMBO J. *33*, 356–370. https://doi.org/10.1002/embj.201386399.
8. Hu, Y.L., Lu, S., Szeto, K.W., Sun, J., Wang, Y., Lasheras, J.C., and Chien, S. (2014). FAK and paxillin dynamics at focal adhesions in the protrusions of migrating cells. Sci. Rep. *4*, 6024. https://doi.org/10.1038/srep06024.
9. Chen, T.H., Chan, P.C., Chen, C.L., and Chen, H.C. (2011). Phosphorylation of focal adhesion kinase on tyrosine 194 by Met leads to its activation through relief of autoinhibition. Oncogene *30*, 153–166. https://doi.org/10.1038/onc.2010.398.
10. Acebrón, I., Righetto, R.D., Schoenherr, C., de Buhr, S., Redondo, P., Culley, J., Rodríguez, C.F., Daday, C., Biyani, N., Llorca, O., et al. (2020). Structural basis of Focal Adhesion Kinase activation on lipid membranes. EMBO J. *39*, e104743. https://doi.org/10.15252/embj.2020104743.
11. Ribeiro-Pereira, C., Moraes, J.A., Souza, M.d.J., Laurindo, F.R., Arruda, M.A., and Barja-Fidalgo, C. (2014). Redox modulation of FAK controls melanoma survival - role of NOX4. PLoS One *9*, e99481. https://doi.org/10.1371/journal.pone.0099481.
12. Giannoni, E., Buricchi, F., Grimaldi, G., Parri, M., Cialdai, F., Taddei, M.L., Raugei, G., Ramponi, G., and Chiarugi, P. (2008). Redox regulation of anoikis: reactive oxygen species as essential mediators of cell survival. Cell Death Differ. *15*, 867–878. https://doi.org/10.1038/cdd.2008.3.
13. Giannoni, E., Buricchi, F., Raugei, G., Ramponi, G., and Chiarugi, P. (2005). Intracellular reactive oxygen species activate Src tyrosine kinase during cell adhesion and anchorage-dependent cell growth. Mol. Cell Biol. *25*, 6391–6403. https://doi.org/10.1128/MCB.25.15.6391-6403.2005.
14. Chiarugi, P., Fiaschi, T., Taddei, M.L., Talini, D., Giannoni, E., Raugei, G., and Ramponi, G. (2001). Two vicinal cysteines confer a peculiar redox regulation to low molecular weight protein tyrosine phosphatase in response to platelet-derived growth factor receptor stimulation. J. Biol. Chem. *276*, 33478–33487. https://doi.org/10.1074/jbc.M102302200.
15. Chiarugi, P., Pani, G., Giannoni, E., Taddei, L., Colavitti, R., Raugei, G., Symons, M., Borrello, S., Galeotti, T., and Ramponi, G. (2003). Reactive oxygen species as essential mediators of cell adhesion: the oxidative

inhibition of a FAK tyrosine phosphatase is required for cell adhesion. J. Cell Biol. *161*, 933–944. https://doi.org/10.1083/jcb.200211118.

16. Stamler, J.S., Lamas, S., and Fang, F.C. (2001). Nitrosylation: the prototypic redox-based signaling mechanism. Cell *106*, 675–683. https://doi.org/10.1016/S0092-8674(01)00495-0.
17. Shafiei, M.S., Lui, S., and Rockey, D.C. (2015). Integrin-linked kinase regulates endothelial cell nitric oxide synthase expression in hepatic sinusoidal endothelial cells. Liver Int. *35*, 1213–1221. https://doi.org/10.1111/liv.12606.
18. Thom, S.R., Bhopale, V.M., Milovanova, T.N., Yang, M., Bogush, M., and Buerk, D.G. (2013). Nitric-oxide synthase-2 linkage to focal adhesion kinase in neutrophils influences enzyme activity and ??2 integrin function. J. Biol. Chem. *288*, 4810–4818. https://doi.org/10.1074/jbc.M112.426353.
19. Gupta, S.K., and Vlahakis, N.E. (2009). Integrin alpha9beta1 mediates enhanced cell migration through nitric oxide synthase activity regulated by Src tyrosine kinase. J. Cell Sci. *122*, 2043–2054. https://doi.org/10.1242/jcs.041632.
20. Hurd, T.R., DeGennaro, M., and Lehmann, R. (2012). Redox regulation of cell migration and adhesion. Trends Cell Biol. *22*, 107–115. https://doi.org/10.1016/j.tcb.2011.11.002.
21. Parri, M., and Chiarugi, P. (2013). Redox molecular machines involved in tumor progression. Antioxid. Redox Signal. *19*, 1828–1845. https://doi.org/10.1089/ars.2012.5040.
22. Rahman, M.A., Senga, T., Ito, S., Hyodo, T., Hasegawa, H., and Hamaguchi, M. (2010). S-nitrosylation at cysteine 498 of c-Src tyrosine kinase regulates nitric oxide-mediated cell invasion. J. Biol. Chem. *285*, 3806–3814. https://doi.org/10.1074/jbc.M109.059782.
23. da Costa, P.E., Batista, W.L., Moraes, M.S., Stern, A., and Monteiro, H.P. (2018). Src kinase activation by nitric oxide promotes resistance to anoikis in tumour cell lines. Free Radic. Res. *52*, 592–604. https://doi.org/10.1080/10715762.2018.1455095.
24. Thomas, D.D., and Wink, D.A. (2017). NOS2 as an emergent player in progression of cancer. Antioxid. Redox Signal. *26*, 963–965. https://doi.org/10.1089/ars.2016.6835.
25. Basudhar, D., Somasundaram, V., de Oliveira, G.A., Kesarwala, A., Heinecke, J.L., Cheng, R.Y., Glynn, S.A., Ambs, S., Wink, D.A., and Ridnour, L.A. (2017). Nitric oxide synthase-2-derived nitric oxide drives multiple pathways of breast cancer progression. Antioxid. Redox Signal. *26*, 1044–1058. https://doi.org/10.1089/ars.2016.6813.
26. Benhar, M., Forrester, M.T., and Stamler, J.S. (2009). Protein denitrosylation: enzymatic mechanisms and cellular functions. Nat. Rev. Mol. Cell Biol. *10*, 721–732.
27. Rizza, S., and Filomeni, G. (2017). Chronicles of a reductase: biochemistry, genetics and physio-pathological role of GSNOR. Free Radic. Biol. Med. *110*, 19–30. https://doi.org/10.1016/j.freeradbiomed.2017.05.014.
28. Liu, L., Hausladen, A., Zeng, M., Que, L., Heitman, J., and Stamler, J.S. (2001). A metabolic enzyme for S -nitrosothiol conserved from bacteria to humans. Nature *410*, 490–494.
29. Wei, W., Li, B., Hanes, M.A., Kakar, S., Chen, X., and Liu, L. (2010). S-nitrosylation from GSNOR deficiency impairs DNA repair and promotes hepatocarcinogenesis. Sci. Transl. Med. *2*, 19ra13. https://doi.org/10.1126/scitranslmed.3000328.
30. Wei, W., Yang, Z., Tang, C.H., and Liu, L. (2011). Targeted deletion of GSNOR in hepatocytes of mice causes nitrosative inactivation of O6-alkylguanine-dna alkyltransferase and increased sensitivity to genotoxic diethylnitrosamine. Carcinogenesis *32*, 973–977. https://doi.org/10.1093/carcin/bgr041.
31. Cañas, A., López-Sánchez, L.M., Peñarando, J., Valverde, A., Conde, F., Hernández, V., Fuentes, E., López-Pedrera, C., de la Haba-Rodríguez, J.R., Aranda, E., and Rodríguez-Ariza, A. (2016). Altered S-nitrosothiol homeostasis provides a survival advantage to breast cancer cells in HER2 tumors and reduces their sensitivity to trastuzumab. Biochim. Biophys. Acta *1862*, 601–610. https://doi.org/10.1016/j.bbadis.2016.02.005.
32. Cirotti, C., Rizza, S., Giglio, P., Poerio, N., Allega, M.F., Claps, G., Pecorari, C., Lee, J.H., Benassi, B., Barilà, D., et al. (2021). Redox activation of ATM enhances GSNOR translation to sustain mitophagy and tolerance to oxidative stress. EMBO Rep. *22*, e50500. https://doi.org/10.15252/embr.202050500.
33. Rizza, S., Cardaci, S., Montagna, C., di Giacomo, G., de Zio, D., Bordi, M., Maiani, E., Campello, S., Borreca, A., Puca, A.A., et al. (2018). S -nitrosylation drives cell senescence and aging in mammals by controlling mitochondrial dynamics and mitophagy. Proc. Natl. Acad. Sci. USA *115*, E3388–E3397. https://doi.org/10.1007/s10986-018-9401-8.
34. Rizza, S., di Leo, L., Mandatori, S., de Zio, D., and Filomeni, G. (2020). Mitophagy contributes to alpha-tocopheryl succinate toxicity in GSNOR-deficient hepatocellular carcinoma. Biochem. Pharmacol. *176*, 113885. https://doi.org/10.1016/j.bcp.2020.113885.
35. Rizza, S., Montagna, C., Cardaci, S., Maiani, E., Di Giacomo, G., Sanchez-Quiles, V., Blagoev, B., Rasola, A., De Zio, D., Stamler, J.S., et al. (2016). S-nitrosylation of the mitochondrial chaperone TRAP1 sensitizes hepatocellular carcinoma cells to inhibitors of succinate dehydrogenase. Cancer Res. *76*, 4170–4182. https://doi.org/10.1158/0008-5472.CAN-15-2637.
36. Piccinini, F., Tesei, A., Arienti, C., and Bevilacqua, A. (2015). Cancer multicellular spheroids: volume assessment from a single 2D projection. Comput. Methods Programs Biomed. *118*, 95–106. https://doi.org/10.1016/j.cmpb.2014.12.003.
37. Galante, J.M., Mortenson, M.M., Bowles, T.L., Virudachalam, S., and Bold, R.J. (2009). ERK/BCL-2 pathway in the resistance of pancreatic cancer to anoikis. J. Surg. Res. *152*, 18–25. https://doi.org/10.1016/j.jss.2008.05.017.
38. Boucher, M.-J., Morisset, J., Vachon, P.H., Reed, J.C., Lainé, J., and Rivard, N. (2000). MEK/ERK signaling pathway regulates the expression of Bcl-2, Bcl-XL, and Mcl-1 and promotes survival of human pancreatic cancer cells. J. Cell. Biochem. *79*, 355–369. https://doi.org/10.1002/1097-4644(20001201)79:3<355::AID-JCB20>3.0.CO;2-0.
39. Xue, Y., Liu, Z., Gao, X., Jin, C., Wen, L., Yao, X., and Ren, J. (2010). GPS-SNO: computational prediction of protein s-nitrosylation sites with a modified GPS algorithm. PLoS One *5*, e11290. https://doi.org/10.1371/journal.pone.0011290.
40. Felline, A., Seeber, M., and Fanelli, F. (2020). webPSN v2.0: a webserver to infer fingerprints of structural communication in biomacromolecules. Nucleic Acids Res. *48*, W94–W103. https://doi.org/10.1093/nar/gkaa397.
41. Sulzmaier, F.J., Jean, C., and Schlaepfer, D.D. (2014). FAK in cancer: mechanistic findings and clinical applications. Nat. Rev. Cancer *14*, 598–610. https://doi.org/10.1038/nrc3792.
42. Downey-Biechler, C., Craig, D.H., More, S.K., and Basson, M.D. (2019). Inside-out signaling through FAK–integrin axis may regulate circulating cancer cell metastatic adhesion. Proc. Natl. Acad. Sci. USA *116*, 19795–19796. https://doi.org/10.1073/pnas.1904767116.
43. Lee, D.S., and Kim, J.-E. (2018). PDI-mediated S-nitrosylation of DRP1 facilitates DRP1-S616 phosphorylation and mitochondrial fission in CA1 neurons. Cell Death Dis. *9*, 869. https://doi.org/10.1038/s41419-018-0910-5.
44. Luo, M., Zhao, X., Chen, S., Liu, S., Wicha, M.S., and Guan, J.-L. (2013). Distinct FAK activities determine progenitor and mammary stem cell characteristics. Cancer Res. *73*, 5591–5602. https://doi.org/10.1158/0008-5472.CAN-13-1351.
45. Tiede, S., Meyer-Schaller, N., Kalathur, R.K.R., Ivanek, R., Fagiani, E., Schmassmann, P., Stillhard, P., Häfliger, S., Kraut, N., Schweifer, N., et al. (2018). The FAK inhibitor BI 853520 exerts anti-tumor effects in breast cancer. Oncogenesis *7*, 73. https://doi.org/10.1038/s41389-018-0083-1.
46. Tanjoni, I., Walsh, C., Uryu, S., Tomar, A., Nam, J.O., Mielgo, A., Lim, S.T., Liang, C., Koenig, M., Sun, C., et al. (2010). PND-1186 FAK inhibitor selectively promotes tumor cell apoptosis in three-dimensional environments. Cancer Biol. Ther. *9*, 764–777. https://doi.org/10.4161/cbt.9.10.11434.

47. Hou, J., Tan, Y., Su, C., Wang, T., Gao, Z., Song, D., Zhao, J., Liao, Y., Liu, X., Jiang, Y., et al. (2020). Inhibition of protein FAK enhances 5-FU chemosensitivity to gastric carcinoma via p53 signaling pathways. Comput. Struct. Biotechnol. J. *18*, 125–136. https://doi.org/10.1016/j.csbj.2019.12.010.

48. Berger, B.T., Amaral, M., Kokh, D.B., Nunes-Alves, A., Musil, D., Heinrich, T., Schröder, M., Neil, R., Wang, J., Navratilova, I., et al. (2021). Structure-kinetic relationship reveals the mechanism of selectivity of FAK inhibitors over PYK2. Cell Chem. Biol. *28*, 686–698.e7. https://doi.org/10.1016/j.chembiol.2021.01.003.

49. Golubovskaya, V., Curtin, L., Groman, A., Sexton, S., and Cance, W.G. (2015). In vivo toxicity, metabolism and pharmacokinetic properties of FAK inhibitor 14 or Y15 (1, 2, 4, 5-benzenetetramine tetrahydrochloride). Arch. Toxicol. *89*, 1095–1101. https://doi.org/10.1007/s00204-014-1290-y.

50. Granados-Principal, S., Liu, Y., Guevara, M.L., Blanco, E., Choi, D.S., Qian, W., Patel, T., Rodriguez, A.A., Cusimano, J., Weiss, H.L., et al. (2015). Inhibition of iNOS as a novel effective targeted therapy against triple-negative breast cancer. Breast Cancer Res. *17*, 25. https://doi.org/10.1186/s13058-015-0527-x.

51. Li, L., Zhu, L., Hao, B., Gao, W., Wang, Q., Li, K., Wang, M., Huang, M., Liu, Z., Yang, Q., et al. (2017). iNOS-derived nitric oxide promotes glycolysis by inducing pyruvate kinase M2 nuclear translocation in ovarian cancer. Oncotarget *8*, 33047–33063. https://doi.org/10.18632/oncotarget.16523.

52. Schindelin, J., Arganda-Carreras, I., Frise, E., Kaynig, V., Longair, M., Pietzsch, T., Preibisch, S., Rueden, C., Saalfeld, S., Schmid, B., et al. (2012). Fiji: an open-source platform for biological-image analysis. Nat. Methods *9*, 676–682. https://doi.org/10.1038/nmeth.2019.

53. Bankhead, P., Loughrey, M.B., Fernández, J.A., Dombrowski, Y., McArt, D.G., Dunne, P.D., McQuaid, S., Gray, R.T., Murray, L.J., Coleman, H.G., et al. (2017). QuPath: open source software for digital pathology image analysis. Sci. Rep. *7*, 16878. https://doi.org/10.1038/s41598-017-17204-5.

54. Zhou, Y., Liu, Y., Hussmann, D., Brøgger, P., Al-Saaidi, R.A., Tan, S., Lin, L., Petersen, T.S., Zhou, G.Q., Bross, P., et al. (2016). Enhanced genome editing in mammalian cells with a modified dual-fluorescent surrogate system. Cell. Mol. Life Sci. *73*, 2543–2563. https://doi.org/10.1007/s00018-015-2128-3.

55. Piccinini, F. (2015). AnaSP: a software suite for automatic image analysis of multicellular spheroids. Comput. Methods Programs Biomed. *119*, 43–52. https://doi.org/10.1016/j.cmpb.2015.02.006.

56. Tiberti, M., Terkelsen, T., Degn, K., Beltrame, L., Cremers, T.C., da Piedade, I., di Marco, M., Maiani, E., and Papaleo, E. (2022). MutateX: an automated pipeline for in silico saturation mutagenesis of protein structures and structural ensembles. Brief. Bioinform. *23*, bbac074. https://doi.org/10.1093/bib/bbac074.

57. Nielsen, S.V., Stein, A., Dinitzen, A.B., Papaleo, E., Tatham, M.H., Poulsen, E.G., Kassem, M.M., Rasmussen, L.J., Lindorff-Larsen, K., and Hartmann-Petersen, R. (2017). Predicting the impact of Lynch syndrome-causing missense mutations from structural calculations. PLoS Genet. *13*, e1006739.

58. Xiang, X., Corsi, G.I., Anthon, C., Qu, K., Pan, X., Liang, X., Han, P., Dong, Z., Liu, L., Zhong, J., et al. (2021). Enhancing CRISPR-Cas9 gRNA efficiency prediction by data integration and deep learning. Nat. Commun. *12*, 3238. https://doi.org/10.1038/s41467-021-23576-0.

59. Ran, F.A., Hsu, P.D., Wright, J., Agarwala, V., Scott, D.A., and Zhang, F. (2013). Genome engineering using the CRISPR-Cas9 system. Nat. Protoc. *8*, 2281–2308. https://doi.org/10.1038/nprot.2013.143.

60. Alkan, F., Wenzel, A., Anthon, C., Havgaard, J.H., and Gorodkin, J. (2018). CRISPR-Cas9 off-targeting assessment with nucleic acid duplex energy parameters. Genome Biol. *19*, 177. https://doi.org/10.1186/s13059-018-1534-x.

61. Loft, A., Alfaro, A.J., Schmidt, S.F., Pedersen, F.B., Terkelsen, M.K., Puglia, M., Chow, K.K., Feuchtinger, A., Troullinaki, M., Maida, A., et al. (2021). Liver-fibrosis-activated transcriptional networks govern hepatocyte reprogramming and intra-hepatic communication. Cell Metab. *33*, 1685–1700.e9. https://doi.org/10.1016/j.cmet.2021.06.005.

62. Peterson, A.C., Russell, J.D., Bailey, D.J., Westphall, M.S., and Coon, J.J. (2012). Parallel reaction monitoring for high resolution and high mass accuracy quantitative, targeted proteomics. Mol. Cell. Proteomics *11*, 1475–1488. https://doi.org/10.1074/mcp.O112.020131.

63. Law, C.W., Chen, Y., Shi, W., and Smyth, G.K. (2014). voom: precision weights unlock linear model analysis tools for RNA-seq read counts. Genome Biol. *15*, R29. https://doi.org/10.1186/gb-2014-15-2-r29.

64. Mounir, M., Lucchetta, M., Silva, T.C., Olsen, C., Bontempi, G., Chen, X., Noushmehr, H., Colaprico, A., and Papaleo, E. (2019). New functionalities in the TCGAbiolinks package for the study and integration of cancer data from GDC and GTEx. PLoS Comput. Biol. *15*, e1006701.

65. Lucchetta, M., da Piedade, I., Mounir, M., Vabistsevits, M., Terkelsen, T., and Papaleo, E. (2019). Distinct signatures of lung cancer types: aberrant mucin O-glycosylation and compromised immune response. BMC Cancer *19*, 824. https://doi.org/10.1186/s12885-019-5965-x.

66. Ovchinnikov, S., Kamisetty, H., and Baker, D. (2014). Robust and accurate prediction of residue–residue interactions across protein interfaces using evolutionary information. Elife *3*, e02030. https://doi.org/10.7554/eLife.02030.

67. Loving, H.S., and Underbakke, E.S. (2019). Conformational dynamics of FERM-mediated autoinhibition in Pyk2 tyrosine kinase. Biochemistry *58*, 3767–3776. https://doi.org/10.1021/acs.biochem.9b00541.

68. Felline, A., Seeber, M., and Fanelli, F. (2022). PSNtools for standalone and web-based structure network analyses of conformational ensembles. Comput. Struct. Biotechnol. J. *20*, 640–649. https://doi.org/10.1016/j.csbj.2021.12.044.

69. Anders, S., Pyl, P.T., and Huber, W. (2015). HTSeq—a Python framework to work with high-throughput sequencing data. Bioinformatics *31*, 166–169. https://doi.org/10.1093/bioinformatics/btu638.

70. Love, M.I., Huber, W., and Anders, S. (2014). Moderated estimation of fold change and dispersion for RNA-seq data with DESeq2. Genome Biol. *15*, 550. https://doi.org/10.1186/s13059-014-0550-8.

STAR★METHODS

KEY RESOURCES TABLE

REAGENT or RESOURCE	SOURCE	IDENTIFIER
Antibodies		
Mouse monoclonal anti-α-Tubulin	Sigma-Aldrich	Cat#T9026; RRID: AB_477593
Goat polyclonal anti-Actin	Santa Cruz Biotechnology	Cat# sc-1616; RRID: AB_630836
Rabbit polyclonal anti-Bcl-2	Cell Signaling Technology	Cat# 2876, RRID: AB_2064177
Rabbit polyclonal anti-Caspase-3	Cell Signaling Technology	Cat# 9662, RRID: AB_331439
Rabbit monoclonal anti-FAK	Cell Signaling Technology	Cat# 13009; RRID: AB_2798086
Mouse monoclonal anti-GAPDH	Millipore	Cat# CB1001, RRID: AB_2107426
Mouse monoclonal anti-GSNOR (ADH5)	Santa Cruz Biotechnology	Cat# sc-293460; RRID: AB_2927735
Mouse monoclonal anti-HA	Sigma-Aldrich	Cat# H3663, RRID: AB_262051
Rabbit monoclonal anti-Ki67	Thermo Fisher Scientific	Cat# RM-9106, RRID: AB_2341197
Rabbit polyclonal anti-LDH	Santa Cruz Biotechnology	Cat# sc-33781, RRID: AB_2134947
Mouse monoclonal anti-Mcl-1	Santa Cruz Biotechnology	Cat# sc-12756, RRID: AB_627915
Rabbit polyclonal anti-NOS2	Santa Cruz Biotechnology	Cat# sc-8310, RRID: AB_2152867
Rabbit polyclonal anti phospho-Paxillin (Y118)	Cell Signaling Technology	Cat# 2541, RRID: AB_2174466
Mouse monoclonal anti-PARP1	Enzo Life Sciences	Cat# BML-SA250-0050, RRID: AB_2052271
Mouse monoclonal anti-Paxillin	Santa Cruz Biotechnology	Cat# sc-365379, RRID: AB_10859206
Rabbit polyclonal anti-phospho-FAK(Y397) for IHC	Bioworld Technology	Cat# BS4617; RRID: AB_2927736
Rabbit monoclonal anti-phospho-FAK(Y397) for WB	Cell Signaling Technology	Cat# 8556, RRID: AB_10891442
Rabbit polyclonal anti-phospho-FAK(Y576) for IHC	Thermo Fisher Scientific	Cat# PA5-104964, RRID: AB_2816437
Rabbit polyclonal anti-phospho-FAK(Y576/577) for WB	Cell Signaling Technology	Cat# 3281, RRID: AB_331079
Rabbit polyclonal anti-phospho-FAK(Y925)	Cell Signaling Technology	Cat# 3284, RRID: AB_10831810
Rabbit monoclonal anti-phospho-Src Family (Y416)	Cell Signaling Technology	Cat# 6943, RRID: AB_10013641
Rabbit monoclonal anti-Src	Cell Signaling Technology	Cat# 2123, RRID: AB_2106047
Rabbit polyclonal anti-thioredoxin 1	Cell Signaling Technology	Cat# 2298, RRID: AB_2211987
Mouse monoclonal anti-vinculin	Sigma-Aldrich	Cat# V4505, RRID: AB_477617
Chemicals, peptides, and recombinant proteins		
N$^{\omega}$-nitro-L-arginine methyl ester hydrochloride (L-NAME)	Sigma-Aldrich	Cat# N5751, CAS:50,903-99-6
z-VAD-FMK	Sigma-Aldrich	Cat# V116, CAS:187,389-52-2
Staurosporine	Sigma-Aldrich	Cat# S6942, CAS:62,996-74-1
1,2,4,5-Benzenetetraamine tetrahydrochloride (Y15)	Sigma-Aldrich	Cat# SML0837, CAS:4506-66-5
Defactinib (DEF)	Selleckchem	Cat# S7654, CAS:1,073,154-85-4
PP2	Cayman Chemical	Cat# 13198, CAS: 172,889-27-9
Dasatinib (DAS)	APExBIO	Cat# A3017, CAS:302,962-49-8
Saracatinib (SAR)	APExBIO	Cat# A2133, CAS:379,231-04-6
N6022	APExBIO	Cat# B1111, CAS:1,208,315-24-5
SpCas9	IDT	Cat# 1081059
Poly(2-hydroxyethyl methacrylate)	Santa Cruz biotechnology	Cat# sc-253284

(*Continued on next page*)

Continued

REAGENT or RESOURCE	SOURCE	IDENTIFIER
Critical commercial assays		
CellTiter-Glo 3D Cell Viability Assay	Promega	Cat# G9681
LIVE/DEAD® Cell Imaging Kit (488/570)	Thermo-Fisher Scientific	Cat# R37601
Click-iT EdU Cell Proliferation Kit for Imaging	Thermo-Fisher Scientific	Cat# C10338
TUNEL Assay Kit-BrdU-Red	Abcam	Cat# ab66110
RNeasy Plus kit	Qiagen	Cat# 74134
Deposited data		
RNAseq raw and analyzed data	This Paper	GEO: GSE211114
FAK1 structure analysis	This Paper	https://github.com/ELELAB/FAK1_SNO
TGCA analysis	This Paper	https://github.com/ELELAB/FAK1_SNO
Experimental models: Cell lines		
Human: HepG2 (hepatocellular carcinoma)	Cell bank IRCCS Ospedale Policlinico San Martino	Cat# ICLC HTL95005
Human: 769-P (renal cell carcinoma)	CLS	Cat# 300106, RRID:CVCL_1050
Human: RD (rhabdomyosarcoma)	CLS	Cat# 300401
Human: HeLa (endocervical adenocarcinoma)	ATCC	Cat# CCL-2, RRID:CVCL_0030
Human: MCF7 (breast adenocarcinoma)	ATCC	Cat# HTB-22
Experimental models: Organisms/strains		
Mouse: NOD.Cg-*Prkdc*^{scid}*Il2rg*^{tm1Sug}/JicTac	Taconic	Cat# 13440-M
Oligonucleotides		
endonuclease-prepared siRNAs against GSNOR	Sigma-Aldrich	Cat# EHU104681
endonuclease-prepared siRNAs against FAK1	Sigma-Aldrich	Cat# EHU077321
endonuclease-prepared non-target siRNAs	Sigma-Aldrich	Cat# SIC001
gRNAs for CRISPr/Cas9 GSNOR-KO generation: GSNOR ex5_SS CACCGTTCACAGCAGCACCATAAC	This paper	N/A
gRNAs for CRISPr/Cas9 GSNOR-KO generation: GSNOR ex5_AS AAACGTTATGGTGCTGCTGTGAAC	This paper	N/A
gRNAs for CRISPr/Cas9 GSNOR-KO generation: GSNOR ex6_SS CACCGTAAAGTGGCTGGTGCTTCC	This paper	N/A
gRNAs for CRISPr/Cas9 GSNOR-KO generation: GSNOR ex6_AS AAACGGAAGCACCAGCCACTTTAC	This paper	N/A
c-check for CRISPr/Cas9 GSNOR-KO validation: c-check Ex5-6_F GTCGGATGTTCACAGCAGCACCATAACCGGGT AAAGTGGCTGGTGCTTCCAGGATAGGT	This paper	N/A
c-check for CRISPr/Cas9 GSNOR-KO validation: c-check Ex5-6_R CGGTACCTATCCTGGAAGCACCAGCCACTTTA CCCGGTTATGGTGCTGCTGTGAACATC	This paper	N/A
gRNA spacer sequences, for FAK1 a.C658S substitution: FAK1-gRNA1 CAGCCTTATGACGAAATGCT	This paper	N/A
gRNA spacer sequences, for FAK1 a.C459A substitution: FAK1-gRNA2 AACATGTAAAAACTGTACTT	This paper	N/A
ssODN for FAK1 a.C658S substitution: G*A*GCTGAGCTTTAAGTTCAGTAAACCTGGGC CGCCTGCTGGGGTCATAGGCCCAGCtcTTaGT CATgAGGCTGTAGAGGGTAGGAGGACAATTTG GAGGCATTGGTAATCTTTCCCCA*T*T	This paper	N/A

(*Continued on next page*)

Continued

REAGENT or RESOURCE	SOURCE	IDENTIFIER
ssODN for FAK1 a.C459A substitution: C*A*GAAATTTCTAGACACTTACAGGCTTCTTG AAGAAATTTCTCTCTCACGCTGTCaGAAGTAg cGTTTTTACATGTTTTAATTGCAACCGCCAAA GCTGGATTCTCCTGTGTTAGGGA*A*A	This paper	N/A
PCR primer for C658S genotyping F1 ATGCTGCTTTGGTAGATAATTTGC	This paper	N/A
PCR primer for C658S genotyping R1 TCAGAAGCTAGGGGAGAGAGATTTG	This paper	N/A
PCR primer for C459A genotyping F1 GATTTGCTGTAATGTTTCACGTGC	This paper	N/A
PCR primers for C459A genotyping R1 GCAGCATCAACATTAGGATCACTT	This paper	N/A
Mutagenic primer: GSNOR R115H_top CCTTTGCCAGAAGATAAAAGTCACTCAAGGGAAAGG	This paper	N/A
Mutagenic primer: GSNOR R115H_bot CCTTTCCCTTGAGTGACTTTTATCTTCTGGCAAAGG	This paper	N/A
Mutagenic primer: FAK1 C459A_top GTAAAAACGCTACTTCGGACAGCGTGAGAG	This paper	N/A
Mutagenic primer: FAK1 C459A_bot CCGAAGTAGCGTTTTTACATGTTTTAATTGCAACC	This paper	N/A
Mutagenic primer: FAK1 C658S_top GACGAAATCCTGGGCCTATGACCCCAG	This paper	N/A
Mutagenic primer: FAK1 C658S_bot GGCCCAGGATTTCGTCATAAGGCTGTAG	This paper	N/A
Recombinant DNA		
Plasmid: pLPCX-GSNOR	This paper	N/A
Plasmid: pLPCX-GSNOR R115H	This paper	N/A
Plasmid: pcDNA3.1-HA-FAK1	This paper	N/A
Plasmid: pcDNA3.1-HA-FAK1 C459A	This paper	N/A
Plasmid: pcDNA3.1-HA-FAK1 C658S	This paper	N/A
Software and algorithms		
ImageJ	Schindelin et al.[52]	RRID:SCR_002285 https://imagej.net/software/fiji/
Graphpad Prism v.9	GraphPad Software	RRID:SCR_002798 https://www.graphpad.com/scientific-software/prism/
Spotfire v10 software	TIBCO	RRID:SCR_008858 https://www.tibco.com/products/tibco-spotfire
Skyline	MacCoss Lab	RRID:SCR_014080 https://skyline.gs.washington.edu/labkey/project/home/software/Skyline/begin.view
QuPath v0.3.0	Bankhead P et al.[53]	RRID:SCR_018257 https://qupath.github.io/

RESOURCE AVAILABILITY

Lead contact

Further information and requests for resources and reagents should be directed to and will be fulfilled by the lead contact, Giuseppe Filomeni (GF) (giufil@cancer.dk).

Materials availability

- This study did not generate new unique reagents.

- Plasmids generated in this studies are reported in the key resources table and are available upon request to the lead contact, GF (giufil@cancer.dk).

Data and code availability

- RNA-seq data have been deposited at GEO and are publicly available as of the date of publication. Accession numbers is listed in the key resources table.
- The authors declare that all data supporting the findings of this study are available within the paper and its supplemental information files. All numeric data used to build histograms and graphs as well as the statistical test used for each experiment are reported in Table S1.
- Original unprocessed and uncut western blot images are reported in Data S1. Microscopy data reported in this paper will be shared by the lead contact upon request.
- The data and scripts for FAK1 modeling and structural analyses, and the analysis of TCGA database are reported in the GitHub repository and public available: https://github.com/ELELAB/FAK1_SNO.
- Any additional information required to reanalyze the data reported in this paper is available from the lead contact upon request

EXPERIMENTAL MODEL AND SUBJECT DETAILS

Cell lines and spheroids

HepG2 cells were obtained from Banca Biologica e Cell Factory (IRCCS AOU San Martino - IST); 769P (clear cell adenocarcinoma) and RD (rhabdomyosarcoma) were purchased from CLS Cell Lines Service GmbH; HeLa and MCF7 cells were purchased from ATCC (American Type Culture Collection). Cells were maintained in a humidified 5% CO_2, 37°C incubator. HeLa, Mcf7, RD cells were grown in Dulbecco's modified Eagle's medium (DMEM), HepG2 and 769P cells were grown in RPMI-1640. Both media were supplemented with 10% fetal bovine serum (FBS) and penicillin-streptomycin (100 U/ml). All cell lines were used from the third to the 15th passage in culture after resuscitation. Cell lines validation was carried out by the producer by means of DNA Profile STR (Short Tandem Repeat) and mycoplasma contamination was routinely screened by a PCR-based assay (Eurofins Genomics). All cell culture media and supplements were purchased from Gibco, Thermo-Fisher Scientific. HepG2 cells stably expressing eGFP-short-hairpin RNAs (shRNA) were generated in our lab with a procedure reported in.[35] HeLa and Mcf7 GSNOR KO cells were generated by CRISPR/Cas9 technology and enriched using the dual-fluorescent surrogate reporter system (c-check) as reported by Zhou et al.[54] Guide RNAs and c-check inserts used are reported in the key resources table.

Forced suspension was induced by growing cells on Poly(2-hydroxyethyl methacrylate)-coated plates (Santa Cruz biotechnology, sc-253284). Spheroids were produced by seeding 750,1500 or 3000 cells/well into ultra-low attachment U-bottom 96-multiwells (Corning, CLS7007-24EA) in standard growing conditions for 7-to-14 days, with 1/3 of the medium refreshed every 3 days. Brightfield images of spheroids were acquired with a Celigo Image Cytometer (Nexcelom Bioscience). ReViSP software was used to compute spheroids 3D surface starting from a brightfield image (http://sourceforge.net/p/revisp/).[36] AnaSP was used to monitor spheroids morphological parameters (diameter and sphericity index).[55]

Experiments showing engineered cell lines (both by CRISPR/Cas9 or shRNAs) have been conducted on mixed populations of at least three different clones to avoid any clonal effect on the phenotype.

Animal model

Animal experiments were conducted on five-week-old male NOD.Cg-*Prkdc*^{scid} *Il2rg*^{tm1Sug}/JicTac mice purchased from Taconic Biosciences A/S. Animals were kept single housed and were allocated to experimental groups randomly. Experiments were licensed by the ethical committee Dyreforsøgstilsynet, The Animal Experiments Inspectorate of the Ministry of Food, Agriculture and Fisheries of Denmark (https://en.dyreforsoegstilsynet.dk) with protocol nr. 2018-15-0201-01391.

METHOD DETAILS

Reagents and treatments

Compounds and concentrations used in the study are as follows: N^{ω}-nitro-L-arginine methyl ester hydrochloride (L-NAME, Sigma-Aldrich, N5751, CAS:50,903-99-6) 500 μM; z-VAD-FMK (ZVAD, Sigma-Aldrich, V116, CAS:187,389-52-2), 20 μM; Staurosporine (STAU, Sigma-Aldrich, S6942, CAS:62,996-74-1), 1 μM; 1,2,4,5-Benzenetetraamine tetrahydrochloride (Y15, Sigma-Aldrich, SML0837, CAS:4506-66-5), 1–10 μM; Defactinib (DEF, Selleckchem, S7654, CAS:1,073,154-85-4), 1–10 μM; 10–50 μM; PP2 (Cayman Chemical, 13,198, CAS: 172,889-27-9) 10 μM; Dasatinib (DAS, APExBIO, A3017, CAS:302,962-49-8) 100 nM; Saracatinib (SAR, APExBIO, A2133, CAS:379,231-04-6) 1 μM; N6022 (APExBIO, B1111, CAS:1,208,315-24-5) 5 μM. Incubation times are indicated in the figure legends.

Transient transfections and plasmids

Transient knock-down was performed by transfecting the cells with RNAiMAX (Thermo Fisher Scientific) endonuclease-prepared pools of siRNAs (esiRNA, Sigma-Aldrich) directed against ADH5 (siGSNOR, EHU104681), PTK2 (siFAK1, EHU077321), or with a scramble duplex (siSCR, SIC001). Overexpression of protein constructs was performed using Polyethylenimine (PEI, Tebu-bio, 23,966-1) in HeLa cells and Lipofectamine 3000 (Thermo Fisher Scientific, L3000001) in HepG2 cells according to manufacturer's instruction. The plasmids used in this work were generated in our laboratory. ADH5 cDNA coding for GSNOR was cloned into the vector pLPCX (Clontech). PTK2 cDNA coding for FAK1 was cloned into the vector pcDNA3.1-HA (Invitrogen). Plasmids encoding for mutant forms of GSNOR and FAK1 were generated by site-directed mutagenesis using the oligos reported in the key resources table. We estimated the effect of mutations at C459 and C658 sites using protocols based on folding free energy calculations with the MutateX energy functions.[56] The changes in folding free energy upon mutations predicted by these approaches correlates with the cellular stability of the protein and it has been shown that mutations with changes of folding free energy lower than 3 kcal/mol result in marginal effects on cellular stability[57]

Generation of FAK1 point mutations in cells

Design and synthesis of CRISPR-SpCas9 gRNAs

gRNA spacers were designed using the deep learning tool CRISPRon.[58] The gRNAs were selected to introduce targeted cleavage as closer to the mutation site as possible to enhance knock-in efficiency. All gRNAs were chemically modified to increase stability in cells and synthesized by Synthego Co. (California).

Design and synthesis single strand oligonucleotides (ssODN)

The ssDNA was designed based on a similar protocol described previously to enhance knock-in efficiency.[59] Briefly, the targeting strand DNA was selected for the ssODN. Second, we selected symmetric homology sequences flanking the desired mutation site. Third, silence mutations were introduced to block the potential re-cutting of the CRISPR on the edited site. And lastly, phosphorothioate (PS) bond modifications were introduced between the last 3 nucleotides at the 5′- or 3′ end of the oligo to inhibit exonuclease degradation. All ssODNs were synthesized by Integrated DNA Technologies, Inc.

Nucleofection of CRISPR Ribonucleoprotein (RNP) and ssODN

The CRISPR RNP and ssODN were delivered into cells by nucleofection. For one nucleofection, 6 μg SpCas9 protein (Cat# 1081059, IDT) and the 3.2 μg synthetic gRNA (Synthego) was mixed in a PCR tube and incubated at room temperature for 10–60 min. Ten minutes after forming the RNP complex, 1 μg ssODN (IDT) was added to the complex. Then 200,000 suspended cells were resuspended in nucleofection buffer (OptiMEM) and the cells and RNP:ssODN complex were transferred to a 4D-Nucleofector 16-well nucleocuvette strip (Catalog #: AXP-1004, Lonza). Nucleofection was performed with program CM-138. The cells were then transferred into one well of a 12-well cell culture plate with prewarm medium.

Generation of single cell colonies and genotyping

48 h after nucleofection, cells were washed with pre-warm PBS and trypsinized (R001100, ThermoFisher Scientific) and single cells were manually picked and transferred to a 96-well cell culture. After the first 5 days, medium was replaced every 3 days for approximately two weeks. Upon 70–80% confluence, the single cell-derived colonies were dissociated in Trypsin-EDTA and 1/3 of the cells were transferred to a PCR tube and used for genotyping. Cells were lysed at 65°C for 30 min, followed 95°C for 10 min in lysis buffer (50 mM KCl, 1.5 mM $MgCl_2$, 10 mM Tris–Cl, pH 8.5, 0.5% Nonidet P40, 0.5% Tween, 400 μg/ml Proteinase K). One μL cell lysate was used for each PCR reaction (Dream taq, EP0701, ThermoFisher Scientific). PCR products were gel purified and Sanger sequenced (Eurofinsgenomics). Deconvolution of indel and knockin alleles in the cell clones were carried using the Synthego ICE program (https://ice.synthego.com).

Prediction and validation CRISPR potential off-targets

Potential CRISPR off-target sites were predicted with CRISPRoff.[60] PCR primers were designed for the top 10 potential off-targets. To validate if off-target cleavage was introduced in the CRISPR edited clones, 1 μL cell lysate of cell clone was used for PCR. PCR produced was gel-purified, followed by Sanger sequencing to evaluate the indels. All PCR primers are showed in key resources table.

Analysis of cell death, viability, and proliferation

Cell viability was quantified after 2 h incubation with resazurin 56 mM in full medium (Alamar Blue, Sigma-Aldrich, R7017) by reading the fluorescence emission at 590 nm with a SpectraMax iD3 (Molecular Devices) plate reader.

Spheroid viability was assessed by CellTiter-Glo 3D Cell Viability Assay (Promega, G9681) following manufacturer's protocol. A Victor X4 plate reader (PerkinElmer) was used to record luminescence.

Apoptosis was evaluated by flow cytometry (FACSCalibur, BD) upon staining of cells with a solution of sodium citrate 1% v/v pH 6.0 (Sigma-Aldrich, 71,402), Triton X-100 1% v/v (Sigma-Aldrich, T8787) and propidium iodide 50 μg/mL (Sigma-Aldrich 81,845) measuring the percentage of sub-G1 cell fraction.

Dead cells within spheroids were revealed by ImageXpress Micro Confocal High-Content Imaging System (Molecular Devices) upon staining of spheroids with LIVE/DEAD Cell Imaging Kit (488/570) (Thermo-Fisher Scientific, R37601) and Hoechst 33,342 (Thermo-Fisher Scientific, 62,249). The percentage of dead cells in MCF7 cells was calculated by Fiji ImageJ imaging software[52] as ratio between red nuclei count (dead) and total number of cells (Hoechst-stained) on image max projections. Acquisition of images and 3D rendering of spheroids was performed using MetaXpress software (Molecular Devices).

Cell proliferation was assayed by seeding $2x10^4$ cells/well in 24-wells plates and staining cell nuclei with Hoechst 33,342 at 24, 48 and 72 h h from seeding. Images were acquired using a Celigo Image Cytometer and nuclei counted using proprietary software (Nexcelom Bioscience).

EdU incorporation and cell cycle analysis were assessed by using Click-iT EdU Cell Proliferation Kit for Imaging, (Thermo-Fisher scientific, C10338). Briefly, cells were grown on coverslips and 24h after seeding were fed with EdU for 30min, then fixed in 4% PFA, washed, counterstained with Hoechst 33,342 and EdU conjugated to Alexa Fluor 488 dye according to producer's protocol. The percentage of EdU incorporation was calculated by imaging cells by a Celigo Image Cytometer and EdU/Hoechst ratio calculated by analyzing images with Fiji ImageJ software.[52] Cell cycle analysis was performed by acquiring for each condition, 20 non-overlapping images of 3 independent experiments using the ScanR screening station (Olympus) and processing them using ScanR Analysis software (Olympus). Scatterplots and calculations were generated with Spotfire software (TIBCO).

Tumorigenesis assays

Focus-forming assays

The ability of HepG2 cells to overgrow and form foci was assayed by seeding cells to confluence and keep them in culture for the subsequent 14 days. Cells were then washed twice with PBS, fixed, and stained with a solution of 20% (v/v) Methanol (WVR) and 0.05% (w/v) Crystal violet (Sigma-Aldrich, C0775) on ice for 10 min. After washing, the plate was let completely dry at room temperature. Pictures were acquired with an Olympus microscope equipped with a 4× objective. The size of foci was calculated using Fiji ImageJ.

Soft agar assay

Anchorage-independent growth was assayed by embedding HeLa cells in agar matrix. Briefly, 1% agar (Sigma-Aldrich, A1296) was melted and cooled at 40°C. After 30 min, the solution was mixed with RPMI 2X (Sigma-Aldrich, R6504) supplemented with 20% FBS and antibiotics. The 1:1 mixture was added to 35 mm cell culture dishes and allowed to cool until agar solidification. Cells were trypsinized and resuspended in a mixture 1:1 of 0.7% Agarose (Thermo-Fisher scientific, 16,500,500) and RPMI 2X supplemented with 20% FBS and antibiotics. Cells were seeded 5000/plate and incubated at 37°C for 14 days. Plates were stained with 0.005% Crystal Violet (w/v). After washing, the plates were dried at room temperature, pictures were acquired with an Olympus microscope equipped with a 4× objective and clones were manual counted.

Western blot analyses

Whole cell protein extracts were obtained by rupturing cells in lysis buffer (50 mM Tris HCl, pH 6.8, 2% SDS, 10% glycerol) followed by denaturation for 10 min at 98°C. Protein extracts from tumor tissues were obtained by disruption in RIPA Buffer (50 mM Tris-HCl pH 7.5, 150 mM NaCl, 1 mM EDTA, 5 mM MgCl2, 1% Triton X-100, 0.25% Sodium Deoxycholate, 0.1% SDS, 5 mM β-glycerophosphate, 5 mM NaF, 2 mM Na3VO4, 1:100 protease inhibitor cocktail) (40:1, v/w) using a Qiagen Tissuelyser II (Qiagen, DE) (frequency 20/s, 2 min) with stainless steel beads and clarification at 15,000 × g for 10 min at 4°C. Proteins were quantified by DC Protein Assay Kit (Bio-Rad, 5,000,116). Extracts were electrophoresed by SDS-PAGE and blotted onto PVDF membrane (Bio-Rad, 1,704,273). Primary antibodies used are listed in key resources table. The specific protein complex, formed upon incubation with specific secondary antibodies (Bio-Rad, anti-mouse 1,706,516; anti-rabbit 1,706,515; anti-goat 5160-2504), was identified using a ChemiDoc MP Imaging System (Bio-Rad), after incubation with Amersham ECL Prime Western Blotting Detection Reagent (GE Healthcare, RPN2236). Images were adjusted for brightness and contrast by Fiji ImageJ imaging software.[52]

Detection of S-nitrosylated proteins (biotin-switch assay)

Prediction of FAK1 cysteines potentially target of S-nitrosylation was achieved by GPS-SNO prediction tool.[39] Alignment of human Src (NP_938033.1) and FAK1 (NP_722560.1) protein sequences was achieved by Jalview v2.11.1.7 software. Protein S-nitrosylation was evaluated by biotin-switch assay as previously described.[33] Briefly, cells were homogenized in HEN buffer (HEPES 25 mM, NaCl 50 mM, EDTA 0.1 mM, NP-40 1%, protease inhibitors, pH 7.4). Free cysteine residues were blocked with S-methyl methanethiosulfonate (MMTS, Thermo-Fisher Scientific, 23,011), diluted 1:10 with a solution containing SDS (2.5% final concentration) and incubated for 15 min at 50°C. Proteins were then precipitated with cold acetone, collected by centrifugation, resuspended in HEN buffer with 1% SDS and incubated with EZ-Link HPDP-biotin (2.5 mg/mL, Thermo-Fisher Scientific, 21,341) in the presence or absence of sodium ascorbate 20 mM. After incubation with the HRP-streptavidin (Cell Signaling, 3999), biotinylated proteins were revealed using the ECL Prime detection system (Amersham). All reagents were purchased by Sigma-Aldrich, unless otherwise specified.

FAK1 immunoprecipitation and mass spectrometry

HA-tagged FAK1 WT or alternatively, FAK1 mutants C459A, C658S and C459A-C658S were overexpressed in HeLa cells for 48 h. Protein extract were obtained in IP Buffer (HEMG: 25 mM HEPES pH 8.0, 12.5 mM MgCl2, 0.1 mM EDTA pH 8.0, 10% Glycerol, 100 mM NaCl, 0.5% Triton X-100). 10 mg of protein lysate were immunoprecipitated overnight with anti-HA antibody (Sigma-Aldrich, H3663) conjugated to Dynabeads Protein G (Thermo-Fisher Scientific, 10-004-D). The immunocomplex was then treated for 30 min with 50 mM DTT or with 400 μM PAPA NONOate (Sigma-Altrich) to stimulate S-nitrosylation and then eluted from beads with 1% SDS. Samples were subjected to biotin-switch assay and enriched by pull-down using Pierce Streptavidin magnetic beads (Thermo-Fisher Scientific, 88,817) followed by 3 washes in 10 mM Tris-HCl ph 7.5. Samples were afterward denaturated using 8M

Guanidinium-HCl for 20min an RT. After diluting Guanidinium-HCl to 1M using 50mM ammonium bicarbonate (pH 8.0), the proteins were subjected to on-beads digestion with LysC (1ug) for 3 h at RT followed by Trypsin (1ug) digestion overnight at RT. Digested peptides were then transfer in a new low-bind Eppendorf tubes and digestion was stopped by acidification (pH < 3.0) using trifluoroacetic acid. After desalting using C18 StageTips, eluates containing the digested peptides were concentrated using a speed-vac and resuspended in 8uL of MS Buffer A (0.5% acetic acid in LC-MS grade water, pH 2.5). At this point digested peptides were analyzed using a very similar method and LC-MS/MS setup as reported,[61] with minor modifications; a Parallel Reaction Monitoring method[62] was optimized specifically for monitoring 12 different FAK1 peptides and their potential modified forms (PRM table). Data analysis and spectra visualization was performed using Skyline software setting Biotin-HPDP and Methyl-thiolation on cysteine as potential modifications.

Nitric oxide detection

Nitric oxide relative quantitation was assayed by incubating cells with Diaminofluorescein (DAF)-FM diacetate 10 μM (Thermo-Fisher Scientific, D23844), for 30 min in serum-free DMEM. Stained cells were washed twice with cold PBS, collected, and analyzed by flow cytometry (FACS Verse, BD-biosciences). NO relative concentration was calculated as DAF-FM relative fluorescence (geometric mean).

Xenograft model and treatments

Animal experiments were conducted on five-week-old male NOD.Cg-*Prkdc*^{scid} *Il2rg*^{tm1Sug}/JicTac mice purchased from Taconic Biosciences A/S.

1) *Treatment-free tumor growth* was assayed by injecting on the right flank of each mouse, at the same time, 5 x10^6 shSCR (n = 6) or shGSNOR (n = 6) HepG2 cells resuspended in 100 μL PBS supplemented with 1 mM EDTA. Mice were monitored three times a week for tumor appearance without applying any treatment. When tumors were detectable (approximately 3 × 3 mm), mice were daily monitored, and tumor size measured using a digital caliper for the following two weeks.
2) *To assess the effect of FAK1 inhibition on tumor growth*, we injected 5 ×10^6 shSCR (n = 14) or shGSNOR (n = 14) HepG2 cells in the right flank of each mouse and waited for tumor appearance. FAK1 inhibitor 14 (Y15; Sigma-Aldrich, SML0837, CAS: 4506-66-5) dosage was established following a pilot experiment in which different doses of Y15 were intraperitoneally (IP) administered for 14 days. Side effects were closely assessed on daily basis, such as general distress and weight loss. The highest dose with least side effects (15 mg/kg) was chosen. When tumors were measurable, without taking into consideration how many days passed from cell injection until tumor appearance, mice were randomized in subgroups and received a daily IP injection of either 15 mg/kg Y15 dissolved in saline solution or saline solution as control (Vehicle), for a total of 14 days. Upon drug administration, mice were monitored daily, and health status assessed by weighing the mice three times a week. Tumors were measured daily using a digital caliper and tumor volumes (V) calculated using the formula:

$$V = \frac{(a \times b^2)}{2}$$

where a and b represent width and length of the tumor, and a>b. Mice were euthanized by cervical dislocation 24 h after the last injection and tumors excised, weighted, sectioned and pieces preserved accordingly in relation to the specific downstream applications.

Immunohistochemistry (IHC)

After collection, tumor pieces were fixed overnight at 4°C in 4% PFA, washed and processed with an STP 120 Spin Tissue Processor (ThermoFisher Scientific, 813,150). Samples were then embedded in paraffin (Hounisen, 2270.6060) using a Microm EC 350 modular tissue embedding center (ThermoFisher Scientific). Sections of 4 μm were cut using an HM325 rotary microtome (ThermoFisher Scientific, 902,100), deparaffinized in xylene and rehydrated. Antigen retrieval was performed at 100°C for 4 min using a microwave in freshly prepared Target Retrieval Solution, Citrate pH 6.0 (Dako, S236984) (for pFAK1^{Y576} and pFAK1^{Y397}) or Tris-EDTA buffer (10 mM Tris base, 1 mM EDTA, 0.05% Tween, pH 9.0) (for Ki67). Endogenous peroxidase activity was blocked in freshly prepared 3% H_2O_2 in PBS for 10 min and sections permeabilized with 0.2% Triton X-100 in PBS/Tween 0.05% (PBS-T) for 10 min. After the washes, sections were blocked in Protein Block Serum-Free (Dako, X0909) for 30 min at room temperature and incubated overnight at 4°C with primary antibodies in antibody diluent (Dako, S0809). IHC staining was visualized using EnVision + System- HRP Labeled Polymer Anti-Rabbit (Dako, K4003) and DAB+ (Dako, K3468). Sections were counterstained with hematoxylin (Dako, S3309) according to manufacturer's instructions, 1% sodium bicarbonate, dehydrated and mounted. Digital images were acquired with a NanoZoomer-XR Digital slide scanner (Hamamatsu, JP) and NDP.view 2 software (v2.8.24) and quantified using QuPath (v0.3.0)[53] to determine percentage of Ki67-positive cells in the total area of the section and the intensity of pFAK1^{Y576} and pFAK1^{Y397}cytosolic signal.

Histological analyses and determination of necrotic areas were determined by a pathologist (F.M.B.) blinded to the experimental conditions.

TUNEL assay

In situ cell death was determined using the TUNEL Assay Kit-BrdU-Red (Abcam, ab66110). Tissue sections were deparaffinized, rehydrated and stained following the manufacturer's instructions. Nuclei were stained with 0.5 μg/mL Hoechst 33,342 for 5 min at RT. Images were acquired with a fluorescent AxIo Imager.A2 microscope (Carl Zeiss) equipped with an AxioCaM HRM (Carl Zeiss) and provided with a ZEISS ZEN microscope software (v2.3) (Carl Zeiss). Areas of cell death were measured using Fiji ImageJ software and normalized on the total area of the tumor for each specimen.

Confocal fluorescence microscopy

Cells were grown on coverslip for 24h and then fixed with 4% paraformaldehyde (Sigma-Aldrich, F8775), incubated with a permeabilization solution (PBS/Triton X-100 0.4% v/v) and blocked for 1 h with a blocking solution (PBS/FBS 10% v/v). Afterward, cells were incubated for 1 h with anti-pPaxillin^{Y118} and anti-Vinculin antibody or with an anti-HA antibody. After three washes in PBS, cells were incubated for 1 h with anti-mouse Alexa Fluor 568 and anti-rabbit Alexa Fluor 488 IgG Secondary Antibodies (Thermo-Fisher Scientific, A10037 and A21206). Filamentous actin was revealed by incubation with Alexa Fluor 488 Phalloidin (Thermo-Fisher Scientific, A12379). Nuclei were stained with Hoechst 33,342. Images of cells were acquired by a LSM800 confocal microscope (Carl Zeiss) equipped with an oil-immersion 63× objective and ZEN microscope software (Carl Zeiss). Fluorescence images were adjusted for brightness, contrast, and color balance by using Fiji ImageJ analysis software. Images were deconvoluted using the software Huygens Professional (Scientific Volume Imaging). Quantification of pPaxillin intensity at the focal adhesions (FAs) was performed on the best focused z stack (0.3 μm) by masking Vinculin-positive areas and computing pPaxillin fluorescence intensity in those regions by Fiji ImageJ imaging software.

Analysis from The Cancer Genome Atlas

We used TCGA cancer types and subtypes with a minimum of five primary tumor (TP) and five normal tissue (NT) samples were used in these analyses, to be in accordance with the minimum requirements used in the differential expression analysis with limma-voom[63]. This resulted in a total of 18 TCGA cancer types and 63 TCGA cancer subtypes for analysis. Subtype groups have been defined in accordance with the guidelines provided by the PanCancerAtlas consortium.[64]

Downloading and pre-processing

We worked on pre-aggregated and pre-processed data from TCGA with the Bioconductor/R package *TCGAbioilnks* version 2.12.5[64] downloaded from the NCI Genomic Data Commons (GDC) portal (https://portal.gdc.cancer.gov) in April 2019, for TCGA cancer types and subtypes. Pre-processing, normalization, and filtering has been applied following a protocol described.[65]

Differential expression analysis

We performed differential expression analysis (DEA) comparing primary tumor (TP) and normal samples (NT) by using *limma + voom* transformation with an empirical Bayes procedure, values of the differentially expressed genes (DEGs) as log2 counts per million (logCPM), as implemented in *TCGAbiolinks*.[64] We included as a source of batch effects the information on the tissue source site (TSS) directly in the design matrix for DEA, as suggested by previous studies.[65] We used a cut-off of 0.05 for the adjusted p value (i.e., False Discovery Rate, FDR) and a cut-off of logarithmic fold change (logFC) cut-off of ±0.5 for up- or down-regulated genes. The data and scripts for analyses of the TCG data are provided in the GitHub repository: https://github.com/ELELAB/FAK1_SNO.

Survival analysis

We used Kaplan-Meier survival analysis to correlate GSNOR mRNA expression with patients' overall survival (OS). We used TCGA clinical patient information on the patient state (dead/alive), days till death and age for the analysis. More details are reported in the GitHub repository. Data from the Kaplan–Meier analysis showed in Figure 1C are available in a public repository from the websites (http://kmplot.com/). All the parameters used to analyze patients' survival and draw the plots are reported in Table S1.

Molecular modeling of FAK1 full-length

We used as a reference for the analysis the three-dimensional (3D) structures of FAK1 from *Gallus gallus* which shares 94.86% of sequence identity when compared to the human variant (PDB: 2J0J). We thus selected this structure since it is the only available including both the catalytic kinase and the FERM domain in the same PDB file. We carried out the refinement of the template structure with PDBREDO, which overall improved the model quality. We used MODELLER version 9.15 to reconstruct the missing residues in disordered loops and model the human sequence (residue 35–686). We included contacts predicted by coevolution for the residues of the activation loop and its surroundings to improve the loop reconstruction. The contacts have been predicted with Gremlin.[66] We generated five models and retained the one with the best DOPE score. Experiments suggest that the loop remains partially solvent-exposed when in presence of the FERM domain,[67] which is what we observed in our models. Finally, we applied Protein Structure Network analyses[68] to the 3D model of FAK1 and calculated the so-called meta-paths for long-range communication. The data and scripts for modeling and structural analyses are reported in the GitHub repository: https://github.com/ELELAB/FAK1_SNO.

RNA sequencing analysis

GSNOR-proficient and KO HeLa cells were grown in adhesion for 48 h. Total RNA was purified using RNeasy Plus kit (Qiagen, 74,134) following producer's protocol. RNAseq analysis was performed by Next Generation Diagnostic srl c/o TIGEM. RNAseq data were analyzed by ROSALIND (https://rosalind.bio/), with a HyperScale architecture developed by ROSALIND, Inc. (San Diego, CA). Reads were trimmed using cutadapt. Quality scores were assessed using FastQC. Reads were aligned to the Homo sapiens genome build GRCh38 using STAR. Individual sample reads were quantified using HTseq[69] and normalized via Relative Log Expression (RLE) using DESeq2 R library.[70] DEseq2 was also used to calculate fold changes and p values and perform optional covariate correction. Hypergeometric distribution was used to analyze the enrichment of pathways, gene ontology, domain structure, and other ontologies. The topGO R library, (https://rdrr.io/bioc/topGO/) was used to determine local similarities and dependencies between GO terms in order to perform Elim pruning correction.

QUANTIFICATION AND STATISTICAL ANALYSIS

Statistical significance of all the data presented in this work was calculated using GraphPad Prism v.9 software. Comparisons were considered significant with $p < 0.05$. Statistical analysis is reported in Table S1.

Cell Reports, Volume *42*

Supplemental information

GSNOR deficiency promotes tumor growth via FAK1 *S*-nitrosylation

Salvatore Rizza, Luca Di Leo, Chiara Pecorari, Paola Giglio, Fiorella Faienza, Costanza Montagna, Emiliano Maiani, Michele Puglia, Francesca M. Bosisio, Trine Skov Petersen, Lin Lin, Vendela Rissler, Juan Salamanca Viloria, Yonglun Luo, Elena Papaleo, Daniela De Zio, Blagoy Blagoev, and Giuseppe Filomeni

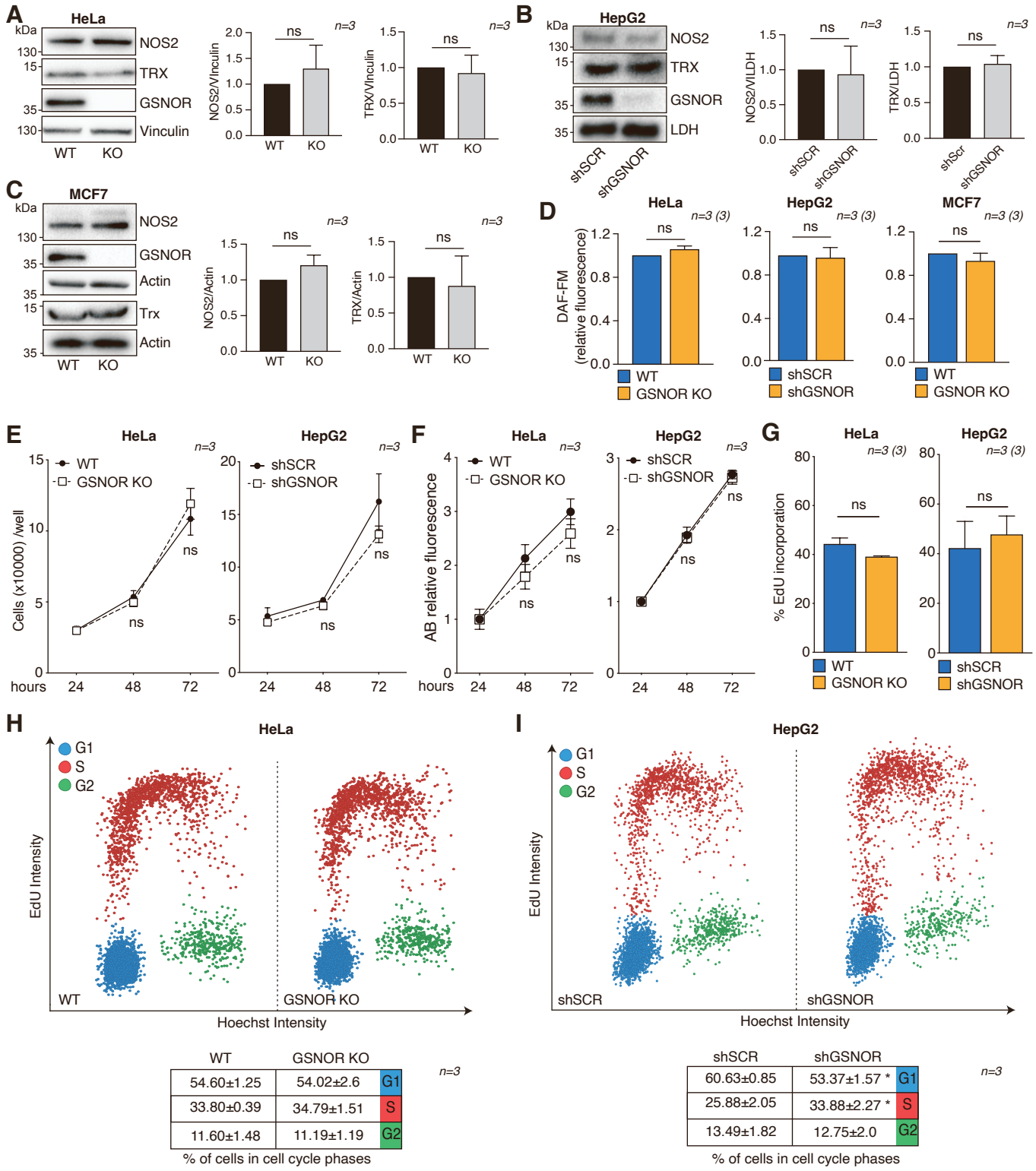

Supplementary Figure 1. GSNOR loss has no effect on NOS2 and TRX expression and does not affect cell proliferation. (Related to Figure 1)

A-C. Western blots of NOS2, thioredoxin (TRX) and GSNOR in extracts from GSNOR-deficient and WT HeLa (**A**), HepG2 (**B**) and MCF7 cells (**C**). Vinculin, LDH or actin were alternatively used

as loading controls. Densitometry is shown on the right. **D.** Flow cytometry determination of free nitric oxide (NO) in GSNOR-deficient and WT HeLa (left), HepG2 (middle) and MCF7 cells (right) upon incubation with DAF-FM. Data are shown as relative fluorescence. **E-F.** Assessment of the total number of cells after Hoechst 33342 nuclei staining (**E**) and cell viability by Alamar Blue (AB) (**F**) of GSNOR-deficient and WT HeLa (left) and HepG2 (right) cells after 24, 48 and 72 h from the seeding. **G.** Percentage of WT and GSNOR-deficient HeLa (left) and HepG2 cells (right) incorporating EdU in 1 h of incubation. **H-I.** Representative scatter plots reporting single-cell EdU and Hoechst intensities in GSNOR-deficient and WT HeLa (**H**) and HepG2 cells (**I**). Cells are coloured according to their cell cycle phase (G1, blue; S, red; G2, green). The percentage of cells ± s.d. in each phase of the cell cycle is reported in the table at the bottom. *n* refers to biologically independent experiments, while numbers in parenthesis represent technical replicates. Histograms represent mean ± s.e.m. (**D, G**) or mean ± s.d. (**A, B, C, E, F**). Data were analysed using two-tailed paired t test (**A, B, C**), unpaired t test (**D, G**), two-way (**E, F**) or one-way (**H**) ANOVA followed by Sidak's multiple comparisons test. ns, not significant; *, $p \leq 0.05$; **, $p \leq 0.01$; ***, $p \leq 0.001$; ****, $p \leq 0.0001$. All raw data and statistics are reported in **Table S1.**

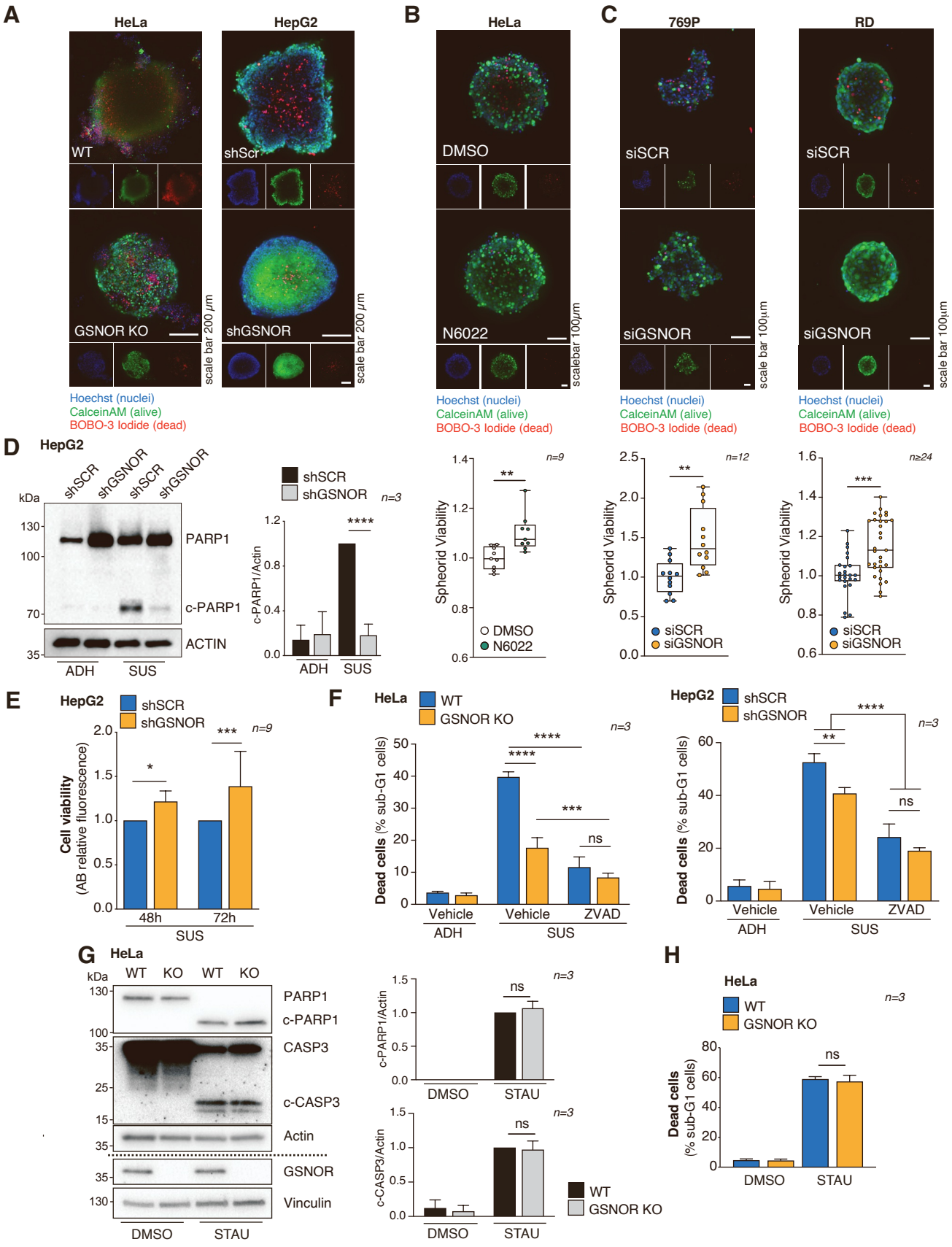

Supplementary Figure 2. GSNOR deficiency results in anoikis resistance without affecting apoptotic machinery. (Related to Figure 2)

A. Representative confocal microscopy images (max projections of ≥10 z-stacks of 10 μm) of GSNOR-deficient vs. WT spheroids generated starting from 3000 HeLa (left) or HepG2 cells (right). Nuclei (blue) were stained by Hoechst 33342, live (green) and dead cells (red) by CalceinAM and BOBO-3 Iodide, respectively. **B.** Representative images (top) of spheroids derived from HeLa cells in the presence of GSNOR inhibitor N6022 5 μM or a control solution (DMSO) acquired and stained as in A. Viability of the spheroids was assessed by CellTiter 3D reagent and expressed as relative luminescence (bottom). **C**. Representative images (top) of spheroids derived from GSNOR-silenced (siGSNOR) and control (siSCR) 769P (left) and RD cells (right) acquired and stained as in A. Viability of the spheroids was assessed by CellTiter 3D reagent and expressed as relative luminescence (bottom). **D.** Western blots of PARP1 and actin in shGSNOR and shSCR HepG2 cells grown in adherence (ADH) or in suspension (SUS) for 72 h. Densitometry is shown on the right. **E.** Cell viability, expressed as Alamar Blue (AB) relative fluorescence, of shGSNOR and shSCR HepG2 cells grown in suspension (SUS) for 48 or 72 h. **F.** Flow cytometry evaluation of SubG1 (dead) cells upon propidium iodide staining of GSNOR-deficient and WT HeLa (left) and HepG2 (right) cells grown in adherence (ADH) or in suspension (SUS) for 48 h with or w/o ZVAD 20 μM. **G-H.** Western blots of PARP1, Caspase-3 (CASP3) and GSNOR (**G**) and flow cytometry evaluation of cell death (**H**) in GSNOR-KO and WT HeLa cells upon treatment with staurosporine 1 μM for 24 h. In immunoblots, actin and vinculin were used as loading control. c- : cleaved forms. Densitometry is shown on the right. *n* refers to biologically independent experiments. Histograms represent mean ± s.d.. In the box plots, centre line shows the median; box limits are the 25th and 75th percentiles; whiskers show minimum and maximum. Data were analysed using two-tailed paired t test (**G**), unpaired t test (**B, C, H**), or one-way ANOVA followed by Sidak's multiple comparisons test (**D, E, F**). ns, not significant; *, $p \leq 0.05$; **, $p \leq 0.01$; ***, $p \leq 0.001$; ****, $p \leq 0.0001$. All raw data and statistics are reported in **Table S1**.

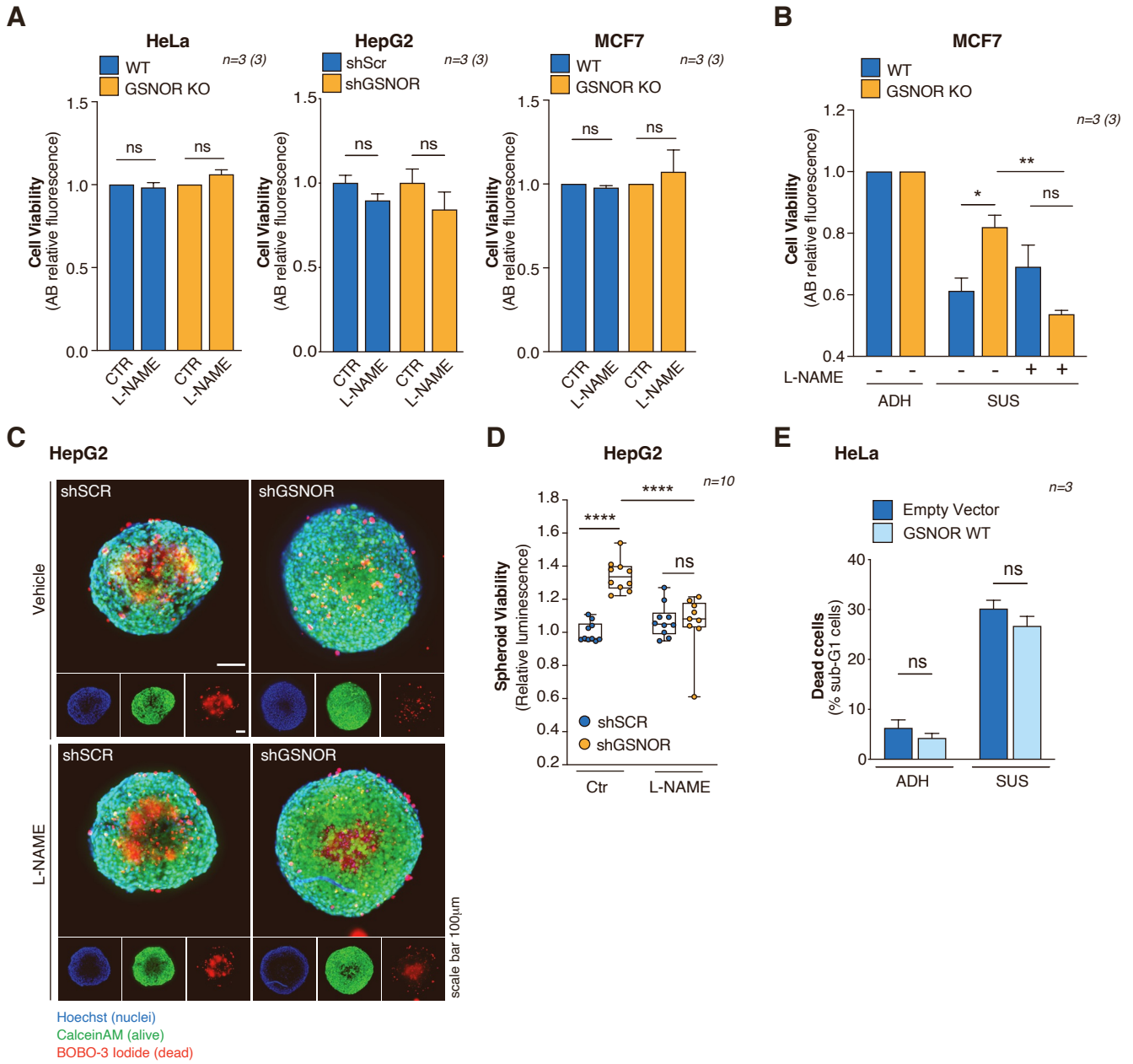

Supplementary Figure 3. The pan-NOS inhibitor L-NAME reverts anoikis resistance of GSNOR-deficient cells. (Related to Figure 3)

A. Cell viability, expressed as Alamar Blue (AB) relative fluorescence, of WT and GSNOR-deficient HeLa (left), HepG2 (middle) and MCF7 cells (right) grown with or w/o L-NAME 500 µM for 48 h. **B.** Cell viability (AB relative fluorescence) of WT and GSNOR-KO MCF7 cells growing in adherence (ADH) or in suspension (SUS) for 48 h in with or w/o L-NAME 500 µM. **C.** Representative confocal microscopy images (max projections of ≥10 z-stacks of 10 µm) of GSNOR-deficient (shGSNOR) vs. control (shSCR) spheroids derived from HepG2 cells treated with L-NAME 500 µM every 48 h for one week. Nuclei (blue) were stained by Hoechst 33342, live (green) and dead (red) cells by CalceinAM and BOBO-3 Iodide, respectively. **D.** Viability of the

spheroids described in **C** was assessed by CellTiter 3D reagent and expressed as relative luminescence. **E.** Flow cytometry evaluation of SubG1 (apoptotic) cells upon propidium iodide staining of HeLa cells transfected with an empty vector or a plasmid encoding for GSNOR WT, grown in adherence (ADH) or in suspension (SUS) for 48 h. *n* refers to biologically independent experiments; numbers in parenthesis represent technical replicates. Histograms represent mean ± s.e.m. (**A, B**) or mean ± s.d. (**E**). In the box plots, centre line shows the median; box limits are the 25th and 75th percentiles; whiskers show minimum and maximum. Data were analysed using one-way (**A, B, D**) or two-way (**E**) ANOVA followed by Sidak's multiple comparisons test. ns, not significant; *, $p \leq 0.05$; **, $p \leq 0.01$; ****, $p \leq 0.0001$. All raw data and statistics are reported in **Table S1**.

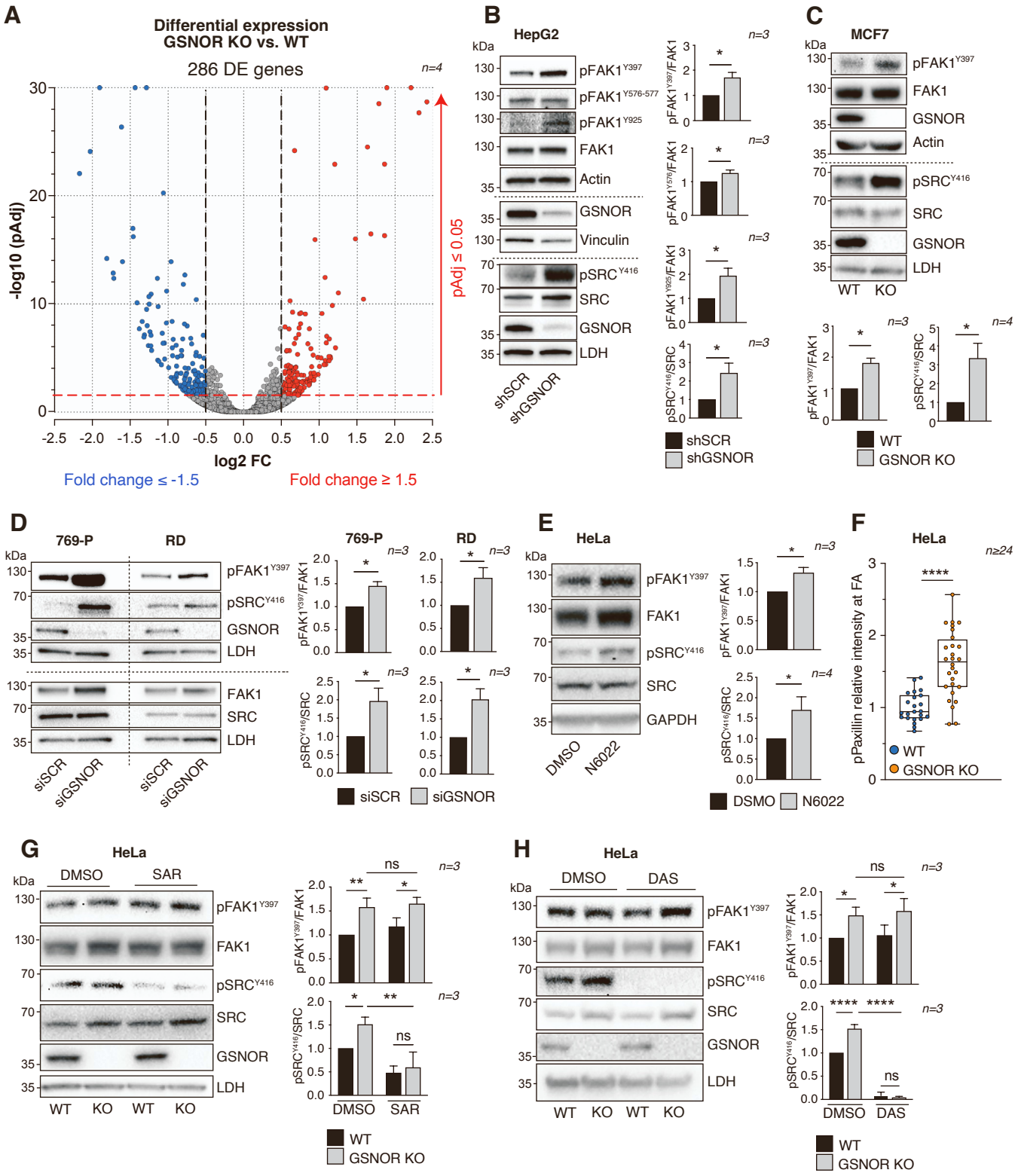

Supplementary Figure 4. GSNOR loss modulates gene expression and stimulates FAK1 signalling. (Related to Figure 4)

A. Volcano plot representation of differential gene expression analysis in GSNOR KO vs. WT HeLa cells. Red and blue points mark the genes (286) with significant increased or decreased

expression in GSNOR KO compared to WT samples, respectively (p-adjusted ≤0.05 and Fold change ≤ -1.5 or ≥ 1.5). The x-axis shows log2 fold-changes in expression and the y-axis the -log10 of p-adjusted of genes differentially expressed. **B-C**. Western blots of GSNOR along with the basal and phosphorylated forms of FAK1 and SCR in WT and GSNOR-deficient HepG2 (**B**) and MCF7 cells (**C**). Vinculin, LDH and actin were alternatively used as loading control. Densitometry is shown on the right (**B**) or in the bottom (**C**). **D**. Western blots of GSNOR along with the basal and phosphorylated forms of FAK1 and SCR in GSNOR-silenced (siGSNOR) and control (siSCR) 769-P (left) and RD (right) cells. LDH was used as loading control. Densitometry is shown on the right. **E**. Western blots of the basal and phosphorylated forms of FAK1 and SCR in HeLa cells upon treatment with N6022 5 μM for 24 h or a control solution (DMSO). GAPDH was used as loading control. Densitometry is shown on the right. **F**. Quantification of the relative intensity of phosphorylated paxillin (pPaxillin) localized at the focal adhesion (FA), revealed by immunofluorescence microscopy as reported in Fig. 3F. **G-H.** Western blots of GSNOR along with the basal and phosphorylated forms of FAK1 and SCR in GSNOR KO and WT HeLa cells upon treatment with saracatinib (SAR) 1 μM (G), dasatinib (DAS) 100 nM (**H**) or a control solution (DMSO) for 24 h. GAPDH was used as loading control. Densitometry is shown on the right. *n* refers to biologically independent experiments. Histograms represent mean ± s.d.. In the box plots, centre line shows the median; box limits are the 25th and 75th percentiles; whiskers show minimum and maximum. Data were analysed using two-tailed paired t test (**B, C, D, E**), unpaired t test (**F**), or one-way ANOVA followed by Sidak's multiple comparisons test (**G-H**). ns, not significant; *, $p \leq 0.05$; ****, $p \leq 0.0001$. All raw data and statistics are reported in **Table S1**.

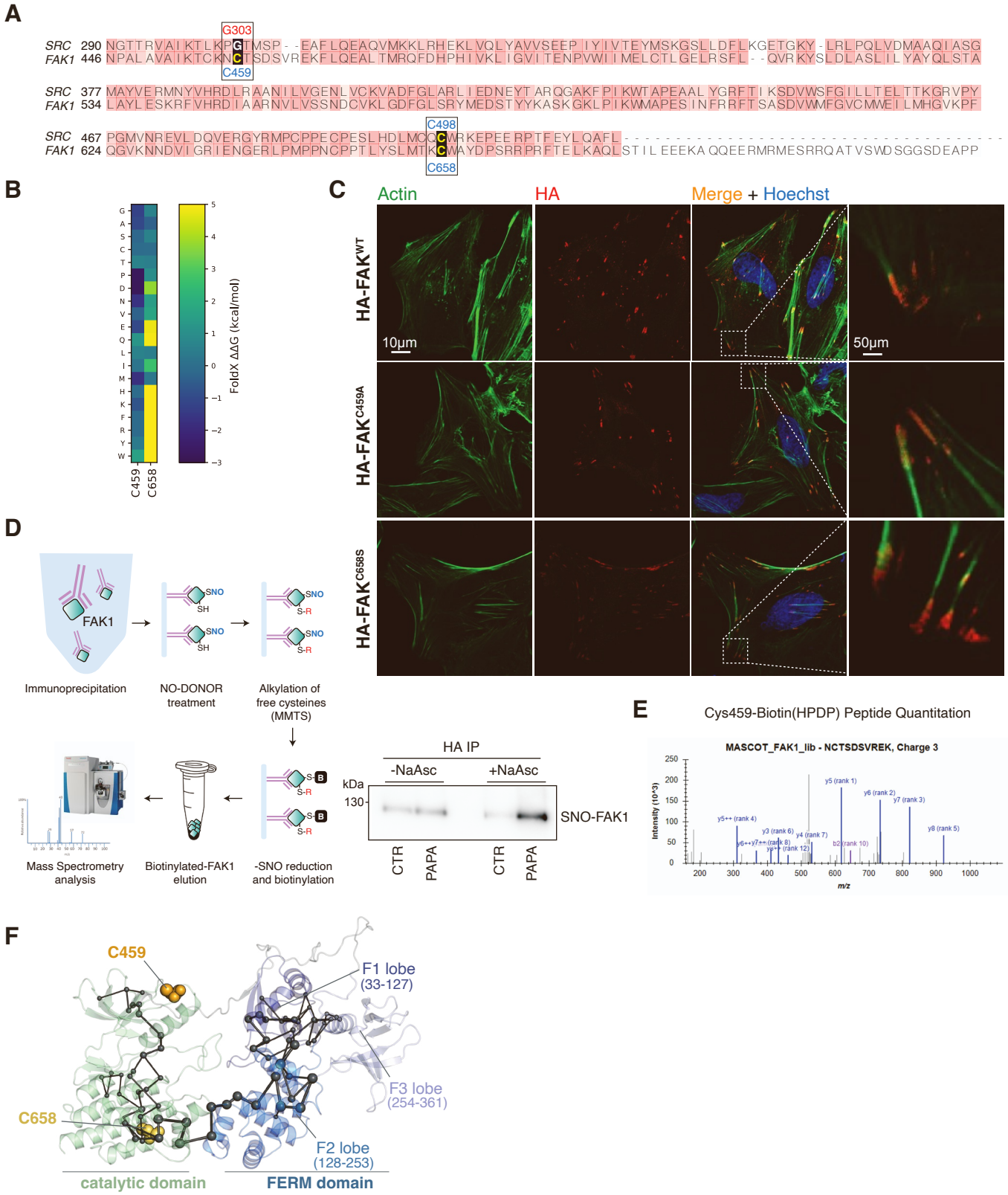

Supplementary Figure 5. Prediction and Mass spectrometry identification of S-nitrosylated cysteines in FAK1. (Related to Figure 5)

A. Detail of the multiple sequence alignment between human SRC (NP_938033.1|) and FAK1 (NP_722560.1). The intensity of pink squares correlates with residue conservation. Cysteines

(Cys) predicted to undergo S-nitrosylation are yellow in a black background and encircled in boxes. **B**. Estimation of the effect of mutations at C459 and C658 sites of FAK1 upon calculation of folding free energy with the FoldX5 energy functions. The heatmap illustrates the predicted $\Delta\Delta G$ values for the saturation mutagenesis scans of the two residues. The amino acids are ordered on the base of their side-chains volumes. Amino acid substitutions that are predicted to be highly destabilizing for the protein are in yellow, while dark purple indicates mutations that are predicted to be stabilizing. **C**. Representative immunofluorescence images of HeLa cells upon 48 h transfection with a plasmid encoding for HA-tagged wild-type FAK1 (HA-FAK^{WT}) or the mutants C459A (HA-FAK^{C459A}) and C658S (HA-FAK^{C658S}) stained with Hoechst 33342 (nuclei, blue), an anti-HA (red) antibody and Alexa Fluor 488 Phalloidin (actin, green). Dotted squares highlight the areas of magnification (5X) on the right. **D.** Schematic representation of sample preparation for mass spectrometry (MS) analysis. Samples were enriched by pull-down with an anti-HA antibody, treated with PAPA, subjected to biotin switch assay, eluted and then analysed by MS. On the right, a representative Western blotting showing S-nitrosylated-FAK1 (SNO-FAK1) revealed in extracts from HeLa cells overexpressing the HA-tagged FAK1, treated with PAPA NONOate 400 μM (30') (PAPA) and subjected to biotin switch assay. **E.** Representative LC/MS-MS spectrum showing SNO-modification at Cys459 of FAK1 as demonstrated by the presence of biotin-Cys label. **F.** 3D structure of FAK1 (residues 35-686) in the autoinhibited state. The catalytic domain is highlighted in green; the FERM domain is highlighted in different shades of blue. The location of F1 (residues 33-127), F2 (residues 128-253), F3 lobe (residues 254-361) of the FERM domain is indicated. S-nitrosylation (SNO) sites C459 and C658 are highlighted in orange and yellow spheres, respectively. The meta-paths analysis is shown as grey links starting from the proximity of SNO sites and connecting the Cα atoms of the residues involved in the allosteric response (grey spheres). The size of grey spheres and links is proportional to their occurrence in the network. The communication from C658 is transmitted to the L2 and L1 lobes of the FERM domain through the interface between the catalytic domain and the L2 lobe. C658 can also propagate structural communication to other distal parts of the catalytic domain.

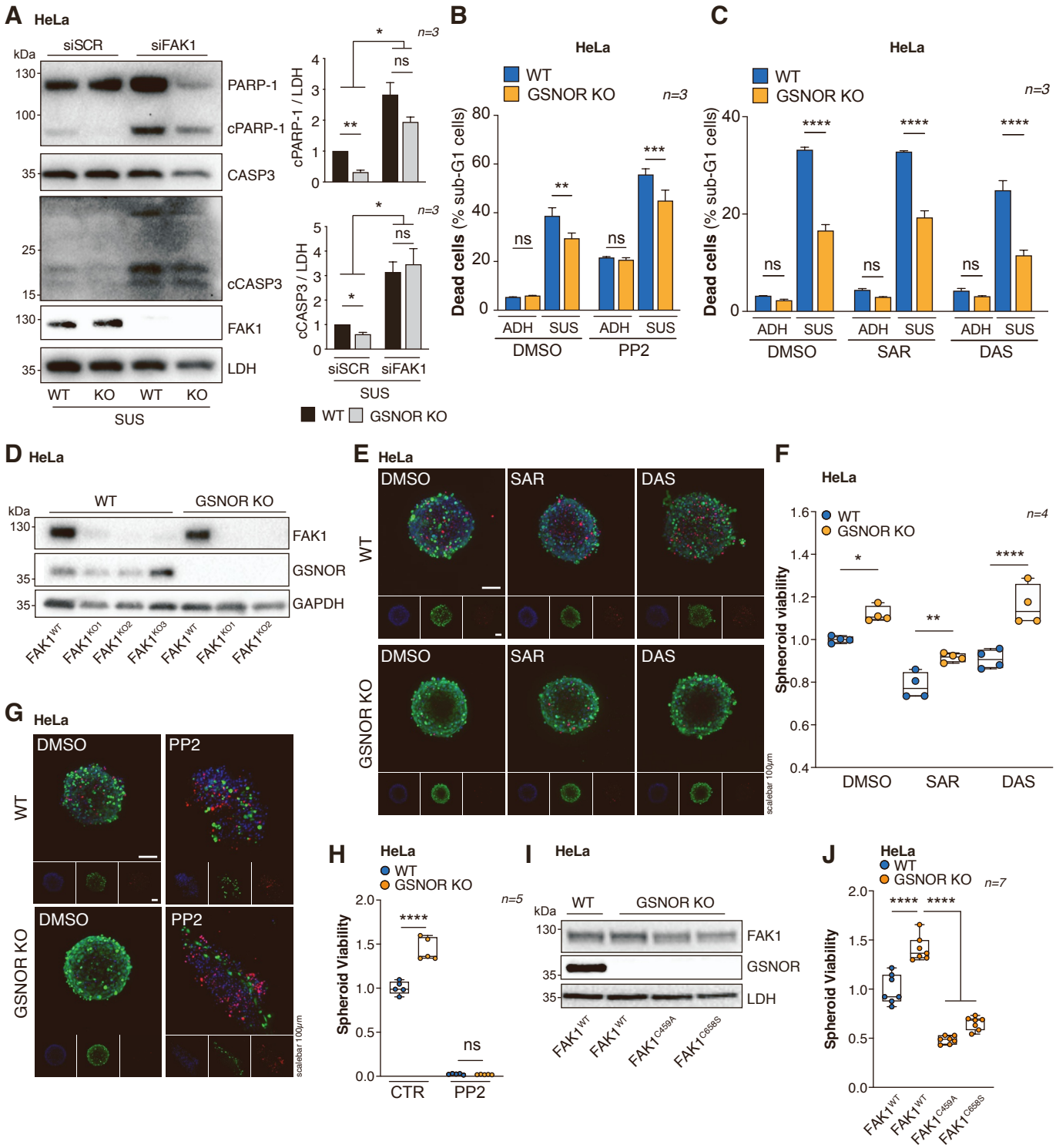

Supplementary Figure 6. Effects of FAK1 depletion or mutagenesis on anoikis and spheroids viability. (Related to Figure 6)

A. Representative Western blot of PARP1, Caspase-3 (CASP3) and LDH in WT and GSNOR-KO HeLa cells transfected with siFAK1 or a non-target RNA interference (siSCR) and grown in suspension (SUS) for 48 h. c-: cleaved forms. Densitometry is shown on the right. **B-C**. Flow

cytometry evaluation of sub-G1 (dead) cells upon propidium iodide staining of GSNOR-deficient (KO) and WT HeLa cells grown in adherence (ADH) or in suspension (SUS) for 48 h in the presence of PP2 5 µM (B), saracatinib (SAR) 1 µM, dasatinib (DAS) 100 nM (**C**) compared to a control solution (DMSO). **D.** Representative Western blot of FAK1 and GSNOR in WT and GSNOR-KO HeLa cells in which endogenous FAK1 was knocked-out by CRISPr/Cas9 technology. GAPDH was used as loading control. **E, G**. Representative confocal microscopy images (max projections of ≥10 z-stacks of 10 µm) of GSNOR-KO vs. WT spheroids generated from HeLa cells in the presence saracatinib (SAR) 1 µM, dasatinib (DAS) 100 nM (**E**) or PP2 5 µM (**G**), compared to a control solution (DMSO). Nuclei (blue) were stained by Hoechst 33342, live (green) and dead cells (red) by CalceinAM and BOBO-3 Iodide, respectively. **F, H**. Viability of the spheroids described in **E (F)** and **G (H)**, assessed by CellTiter 3D reagent and expressed as relative luminescence. **I**. Representative Western blot of FAK1 and GSNOR in WT and GSNOR-KO HeLa cells in which endogenous FAK1 was mutagenized to C459 and C659 by CRISPr/Cas9 technology. LDH was used as loading control. **J**. Box blot showing the viability of spheroids derived from WT, GSNOR-KO, GSNOR-KO endogenously expressing FAK1 C459A or FAK1 C658S HeLa cells assessed by CellTiter 3D reagent and expressed as relative luminescence. *n* refers to biologically independent experiments. Histograms represent mean ± s.d.. In the box plots, centre line shows the median; box limits are the 25th and 75th percentiles; whiskers show minimum and maximum. Data were analysed using one-way ANOVA followed by Tukey's multiple comparisons test (**A, J**) or Šídák's multiple comparisons test (**F, H**), two-way ANOVA followed by Šídák's multiple comparisons test (**B, C**). ns, not significant; *, $p \leq 0.05$; **, $p \leq 0.01$, ***, $p \leq 0.001$; ****, $p \leq 0.0001$. All raw data and statistics are reported in **Table S1**.

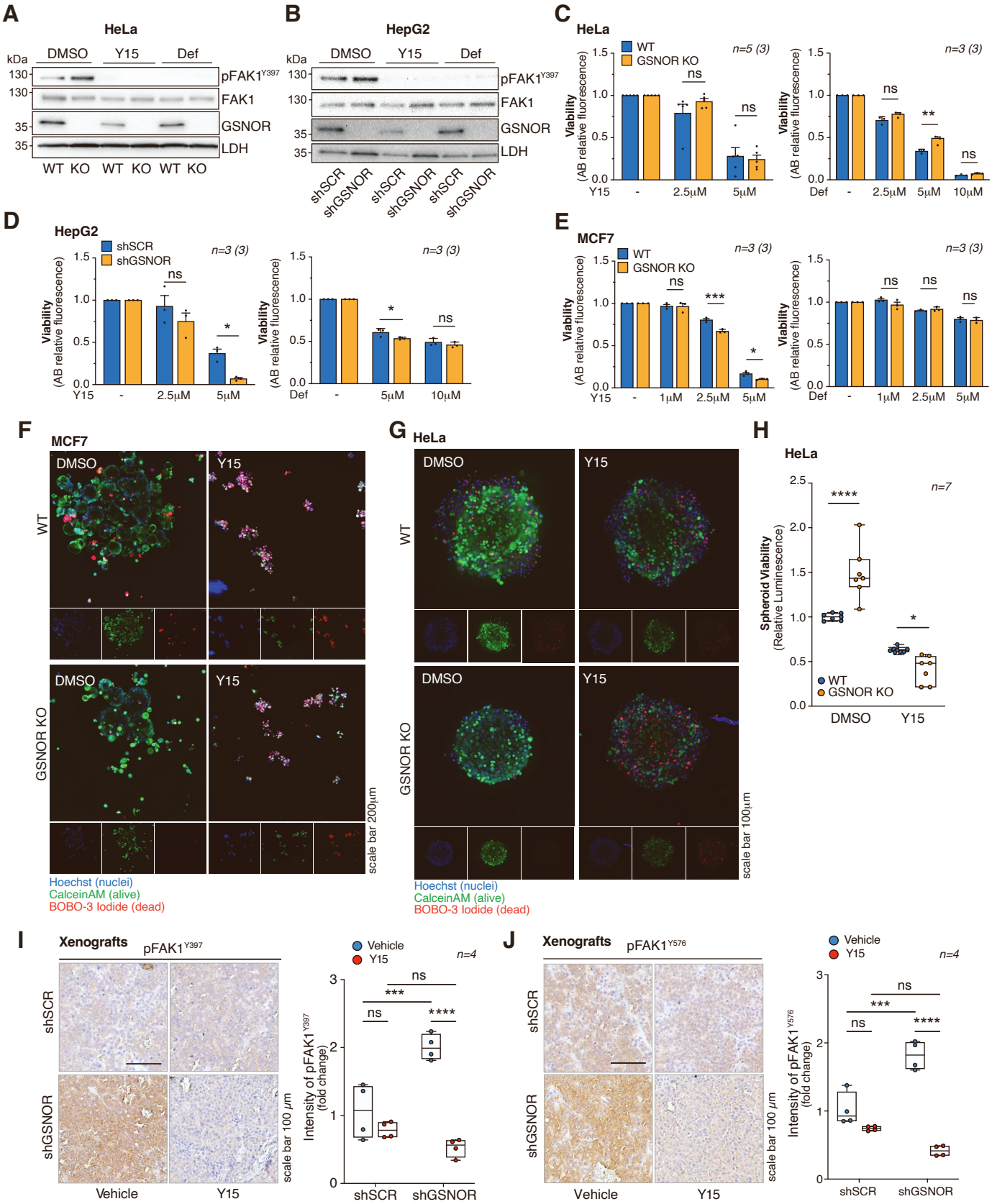

Supplementary Figure 7. FAK1 inhibitors reduces FAK1 phosphorylation and viability in WT and GSNOR-KO tumor models. (Related to Figure 7)

A-B. Western blot of GSNOR and basal and phosphorylated form of FAK1 at Y397 in extracts from HeLa (**A**) and HepG2 cells (**B**) upon 4 h of treatment with Y15 5 μM or Defactinib (DEF) 10 μM. DMSO was used as a vehicle and LDH as loading control. **C-E.** Cell viability, expressed as Alamar Blue (AB) relative fluorescence, of WT and GSNOR-deficient HeLa (**C**), HepG2 (**D**) and MCF7 cells (**E**) treated with Y15 or DEF for 24 h at the indicated concentrations. **F-G.** Representative confocal microscopy images (max projections of ≥10 z-stacks of 10 μm) of WT vs. GSNOR-deficient spheroids generated from MCF7 (**F**) and HeLa cells (**G**) treated every 48 h for one week with Y15 2.5 μM (**F**) or 1 μM (**G**). Nuclei (blue) were stained by Hoechst 33342, live (green) and dead (red) cells by CalceinAM and BOBO-3 Iodide, respectively. **H.** Viability of the spheroids described in g assessed by CellTiter 3D reagent and expressed as relative luminescence. **I-J**. Immunohistochemistry analyses of FAK1 phosphorylated at Y397 (pFAK1^{Y397}) (**I**) and Y576 (pFAK1^{Y576}) (**J**) in tissue sections derived from shGSNOR and shSCR HepG2 xenografts treated with Y15 or a vehicle (saline solution) for 14 days. Right: in-section quantification of pFAK1^{Y397} and pFAK1^{Y576} intensities expressed as fold change. *n* refers to biologically independent experiments; numbers in parenthesis represent technical replicates. Histograms represent mean ± s.e.m. In the box plots, centre line shows the median; box limits are the 25th and 75th percentiles; whiskers show minimum and maximum. Data were analysed using one-way ANOVA followed by Sidak's multiple comparisons test. ns, not significant; *, $p \leq 0.05$; **, $p \leq 0.01$; ***, $p \leq 0.001$; ****, $p \leq 0.0001$. All raw data and statistics are reported in **Table S1**.